PHYSICAL REVIEW A **110**, 012617 (2024)

Quantum circuit model for discrete-time three-state quantum walks on Cayley graphs

Rohit Sarma Sarkar [1,*] and Bibhas Adhikari [2,†]
[1] *Department of Mathematics, Indian Institute of Technology Kharagpur, Kharagpur 721302, India*
[2] *Fujitsu Research of America, Inc., Santa Clara, California 95054, USA*

(Received 25 January 2024; accepted 3 July 2024; published 23 July 2024)

We develop qutrit circuit models for discrete-time three-state quantum walks on Cayley graphs corresponding to dihedral groups D_N and the additive groups of integers modulo any positive integer N. The proposed circuits comprise of elementary qutrit gates such as qutrit rotation gates, qutrit-X gates and two-qutrit controlled-X gates. First, we propose qutrit circuit representation of special unitary matrices of order three, and the block diagonal special unitary matrices with 3×3 diagonal blocks, which correspond to multicontrolled X gates and permutations of qutrit Toffoli gates. We show that one-layer qutrit circuit model needs $O(3nN)$ two-qutrit control gates and $O(3N)$ one-qutrit rotation gates for these quantum walks when $N = 3^n$. Finally we numerically simulate these circuits to mimic its performance such as time-averaged probability of finding the walker at any vertex on noisy quantum computers. The simulated results for the time-averaged probability distributions for noisy and noiseless walks are further compared using KL divergence and total variation distance. These results show that noise in gates in the circuits significantly impacts the distributions than amplitude damping or phase damping errors.

DOI: 10.1103/PhysRevA.110.012617

I. INTRODUCTION

Quantum computing has acquired stellar progress over recent years showcasing quantum algorithms can have more than polynomial speedups compared to their classical counterparts. Hence, developing new efficient quantum algorithms has been a perceptible goal for researchers over the years. Quantum walks, a quantum analog of classical random walks, represent a universal model for quantum computation [1–4] and act as a great platform for designing fast quantum algorithms. Indeed, it is important to highlight that there is currently no established method for converting any quantum algorithm into a quantum walk framework. However, for quantum algorithms where their implementation using quantum circuits is not straightforward, leveraging the quantum circuit model of the quantum walk associated with the algorithm offers a way to implement the quantum algorithm on quantum hardware, such as noisy intermediate scale quantum (NISQ) computers.

Similar to its classical counterpart, quantum walks on graphs are divided into two models based on nature of time evolution viz. discrete-time quantum walks (DTQWs) and continuous-time quantum walks (CTQWs) [5,6]. Apart from the difference in time evolution, DTQWs act on a larger Hilbert space on account of requiring a quantum coin operator, which defines the evolution dynamics of the walker. Several works analyzing fundamental properties of DTQWs (viz. periodicity and localization) exist for three-state DTQWs on several graphs such as lines, cycles, mixed paths or cycles, and Cayley graphs of non-Abelian groups viz. symmetric and dihedral groups [7–12]. In Refs. [13,14], the authors study DTQWs on Cayley graphs of dihedral groups along with their variants. For a detailed review on quantum walks, see Ref. [6]. It is also of note that the discrete-time quantum walks spread quadratically faster in position space in comparison to classical random walks [6,15].

In order to study quantum walks, we approach it through the quantum circuit model of quantum computation. In particular, we will consider qutrit circuits as opposed to the primarily used qubit circuits to incorporate the degree of freedom provided by the three-dimensional quantum coin in our model. Over the years, one of the primary focus in research has been directed towards construction of efficient circuits for the quantum walk model. It is of note that unlike binary system of classical computers, superconducting [16] and trapped ion computers [17] theoretically posses discrete energy levels of an infinite spectrum, which in turn, makes them eligible to work on qudit systems. Many quantum walks related experiments have been carried out on real quantum hardware using qubits [16–20]. However, it is still a challenge to carry out the same experiments efficiently on qutrits and in turn, qudits [21]. Regardless, qutrit circuit model has been the object of interest for researchers worldwide and treated as an alternative to qubit circuits on account of requiring less resources [22,23]. Hybrid quantum circuits using intermediate qutrits instead of qubits and used for efficient decomposition of n-qubit unitary gates has been proposed recently [22,24]. It has been observed that a logarithmic depth can be achieved for circuit synthesis of various unitaries in order to obtain an exponential reduction and requires a 70 times less number of two-qudit gates as compared to two-qubit (CNOT) gates. Further, qutrit-based processors has been theoretically able to demonstrate error correction with small code size [25,26] and it is also theorized to have significant impact in high-fidelity

---

[*] Contact author: rohit15sarkar@yahoo.com

[†] Contact author: badhikari@fujitsu.com

magic state distillation [27], and robust quantum cryptography [28,29] and communication protocols [30]. A recent robust benchmarking has been carried out on a five-qutrit processor showing very low single-qutrit gate infidelity [31]. Works pertaining to constructing circuits of quantum walks exist in literature [32] and this has been extended to developing qutrit circuits for three-state lazy quantum walk on the line [33] and qudit circuits on a lattice for d-state DTQWs [34]. Works also exist in literature showcasing generalizations of certain quantum algorithms (viz. Shor's algorithm, Deustch-Josza algorithm) using qutrits [35–37]. Recently a formulation of QAOA for solving graph three coloring has been proposed using qutrits, which showcase a significant decrease in circuit depth and entangling gates per layer of the QAOA circuit [38]. Moreover, synthesis of certain qudit gates can be found in Ref. [39].

Two-state DTQWs on cycle graphs using Hadamard coin was first introduced in Ref. [1], where the authors studied the limiting behavior of the walk. A three-state DTQW, known as lively quantum walk on cycle graphs was introduced in Refs. [9,40]. Periodicity property of these walks using a general coin has been studied in Ref. [41]. One-dimensional DTQWs on Cayley graphs of dihedral groups using the Hadamard coin was first proposed by Dai *et al.* [42]. This was further extended to three-state DTQW on Cayley graphs of dihedral groups by Liu *et al.* [11] using Grover coin, in which they studied the time-averaged probability of the walk. Recently, we have explored the periodicity and localization properties of DTQWs on Cayley graphs corresponding to dihedral groups for generalized Grover coins in Ref. [12]. Another model of DTQW that is studied recently include DTQWs for Cayley graphs of symmetric groups [7]. Other similar models of quantum walks such as quantum walks on graphs that are generated by free groups and virtually abelian quantum walks are analyzed in Refs. [43,44]. Works involving study of periodicity and localization of DTQWs in line graphs, mixed paths, and cycles can be found in Ref. [10]. For we detailed surveys on DTQWs and DTQWs on Cayley graphs, see Ref. [6].

In this paper, we develop qutrit quantum circuit models for three-state DTQWs on Cayley graphs corresponding to dihedral group D_N and additive groups of integers modulo a positive integer N, where $3^{n-1} < N \leqslant 3^n$ for some positive integer $n \geqslant 1$. For both the graphs, we consider the quantum coins as arbitrary (special) unitary matrices of order 3. We note that Cayley graphs of D_N and $\mathbb{Z}_N$ though planar in nature, are not necessarily undirected. Hence, this work provides qutrit circuit models for quantum walks on mixed (containing both undirected and directed edges) planar graphs. The quantum circuits are defined through some elementary qutrit gates, which include one-qutrit rotation gates and two-qutrit controlled gates. A detailed analysis of circuit complexity of the models is also given. The quantum circuits thus obtained are numerically simulated based on well-known noise models in order to investigate the performance of the circuit models in noisy quantum computers by setting the coin operators as generalized Grover coins, which are one-parameter one-qutrit gates and can be expressed as linear sum of permutation matrices. Since near-term quantum computers are prone to noise, we incorporate varying degrees of error from very high $O(10^{-2})$ to low (10^{-6}) orders of magnitude and numerically observe how much does the erroneous time-averaged probability distribution deviate from that obtained via the ideal noiseless quantum circuit. We infer from our observation that gate noises have a significant impact on the circuit as compared to idle errors. We reproduce the localization property of these walks that exist in literature through the developed circuit models and also review the changes in the time-averaged probability of finding the walker on the vertices of the graphs due to the noises. We notice that the errors are to be kept below $O(10^{-6})$ for the erroneous time-averaged probability to achieve low deviation with respect to its noiseless counterpart. This analysis has promising impact on error mitigation strategies for practical implementation of the proposed quantum circuit models in near-term quantum computers.

The developed circuit models require quantum circuit representation of generic one-qutrit gates that are special unitary matrices, block unitary matrices with 3×3 diagonal blocks that are special unitary matrices, and we provide a mechanism for decomposing multicontrolled qutrit gates into elementary qutrit gates, i.e., we provide a decomposition of generic one-qutrit gates into sequence of qutrit gates that can be viewed as an analog of ZYZ decomposition of special unitary matrices of order 2. We further develop a scalable quantum circuit implementation of block diagonal unitary matrices, which correspond to multicontrolled qutrit gates.

The rest of the paper is organized as follows. In Sec. II, we review the definitions and related mathematical details of DTQWs on the Cayley graphs corresponding to D_N and $\mathbb{Z}_N$, and on elementary qutrit gates. Section III addresses the quantum circuit implementation of generic special unitary matrices of order 3, qutrit circuit models for the DTQWs. The scalable quantum circuit representation of block diagonal unitary matrices and representing multicontrolled qutrit gates into elementary qutrit gates are given in Sec. IV. The circuit complexity of the developed circuit model for the DTQWs is also given in this section. Finally, we report the numerical simulation results in Sec. V.

II. PRELIMINARIES

In this section, we briefly discuss Cayley graphs and the DTQW models on these graphs from Refs. [11,12,42,45]. Then we provide an overview of qutrit gates that are building blocks in the construction of quantum qutrit circuit models for the DTQWs.

A. Cayley graphs

Given a group $(G, \circ)$ and a generating set $H \subseteq G$ of G, the Cayley graph corresponding to the pair (G, H) is defined as $\text{Cay}(G, H) = (V, E)$ where V is the set of vertices in G and two elements $a, b \in V$ are linked by a directed edge from a to b if $b = a \circ c$ for some $c \in H$ and this edge is denoted by (a, b) [45]. In particular, if $c = c^{-1}$ then the edge is both way directed and hence we call it an undirected edge. Hence, for underlying commutative groups, the corresponding Cayley graphs are undirected.

For instance, if $G = \mathbb{Z}_N$, the additive group of integers modulo N and $H = \{1, -1\}$ then $\text{Cay}(\mathbb{Z}_N, \{1, -1\})$ is the undirected cycle graph on N vertices. As an example we

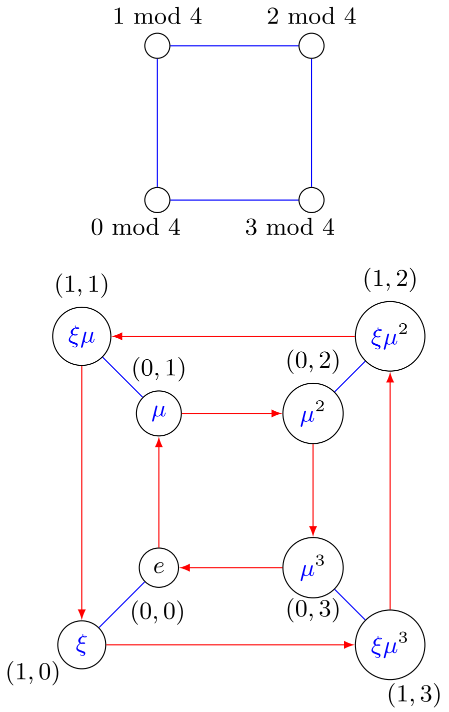

FIG. 1. Cay($\mathbb{Z}_4, \{1, -1\}$) (top) and Cay($D_4, \{\mu, \xi\}$) (bottom).

exhibit a cycle graph with four vertices or Cay($\mathbb{Z}_4, \{1, -1\}$) in Fig. 1.

For a positive integer N, a dihedral group G is defined by two elements, say μ, ξ called the generators of G such that $\xi^2 = \mu^N = e$, the identity element of the group and $\mu\xi\mu = \xi$. From now onward, we denote this dihedral group as $D_N = \langle\{\mu, \xi\}\rangle$. Geometrically, D_N is the group of symmetries of the regular N-gon [45]. The elements of D_N is denoted as $b^s a^r$, where $s \in \{0, 1\}$, $r \in \{0, 1, \dots, N-1\}$, and b represents reflection about an axis of symmetry and the element a represents a rotation by an angle of $\frac{2\pi}{N}$ about the center. If $s = 0$, the N-gon admits rotation and the N-gon admits a reflection if $s = 1$. Clearly, D_N has $2N$ elements which can be labeled as the ordered pairs (s, r), $0 \leqslant s \leqslant 1$, $0 \leqslant r \leqslant N-1$, with $\{\mu, \xi\}$ a generating subset of D_N. The Cayley graph Cay($D_N, \{\mu, \xi\}$) is a mixed graph meaning there exist directed edges between vertices μ^r and μ^{r+1}, i.e., $\mu^r \to \mu^{r+1}$ along with $\xi\mu^{r+1} \to \xi\mu^r$. Further the undirected edges exist between the vertices ξ^r and $\xi\mu^r$, for all $0 \leqslant r \leqslant N-1$. We provide a labeling of the vertices, which is (s, r), $s \in \{0, 1\}$, $r \in \{0, 1, \dots, N-1\}$ as described above. Then Cay($D_N, \{\mu, \xi\}$) can be depicted as two concentric directed cycle graphs possessing opposite orientations, where the vertices of the inner and outer cycle graphs are given by $(0, r)$ and $(1, r)$, respectively, and the undirected edges link the vertices $(0, r)$ with $(1, r)$. For example, in Fig. 1, we exhibit Cay($D_4, \{\mu, \xi\}$).

B. Discrete-time quantum walks on Cay($\mathbb{Z}_N$, {1, −1}) and Cay(D_N, {μ, ξ})

A DTQW on a graph is governed by a unitary operator $U = S(C \otimes I)$, which is applied repeatedly over time to the initial state $|\psi(0)\rangle$ of the walker. The operator S is called the shift operator and C is called the coin operator. Hence U acts on the space $\mathcal{H}_C \otimes \mathcal{H}_p$ where $\mathcal{H}_C$ is the coin space whose dimension gives the internal degree of freedom of the quantum coin associated with the quantum walk and $\mathcal{H}_p$ is the position space spanned by the quantum states localized at the vertices of the graph. Here $\otimes$ denotes the tensor product between vector spaces. The state of the quantum walk at time t for an initial state $|\psi(0)\rangle$ is given by $|\psi(t)\rangle = U^t |\psi(0)\rangle$.

Below we review the DTQWs on Cay($\mathbb{Z}_N, \{1, -1\}$) and Cay($D_N, \{\mu, \xi\}$) from Refs. [11,12] and [9,41], respectively.

1. *Three-state lively quantum walk model on Cay($\mathbb{Z}_N$, {1, −1})*

The vertices of the cycle graph Cay($\mathbb{Z}_N, \{1, -1\}$) can be represented as m, where $0 \leqslant m \leqslant N-1$ and there are undirected edges between the vertices labeled m and $m \pm 1$. The lively DTQW was first introduced in Ref. [40] using the Grover coin. Later, we explored the periodicity properties of these walks in Ref. [41] by considering the coin operators as generalized Grover coins.

The lively DTQW on cycle graph [41] is defined on the Hilbert space $\mathcal{H} = \mathcal{H}_C \otimes \mathcal{H}_V \in \mathbb{C}^3 \otimes \mathbb{C}^N$ where $\mathcal{H}_C = \text{span}\{|0\rangle_3, |1\rangle_3, |2\rangle_3\}$ such that $\{|l\rangle_3 \,|l = 0, 1, 2\}$ is the canonical basis of $\mathbb{C}^3$, the coin space and $\mathcal{H}_V$ is the Hilbert space spanned by the vertices $|m\rangle_N \in V$, $0 \leqslant m \leqslant N-1$ of the cycle graph Cay($\mathbb{Z}_n, \{1, -1\}$), which are, in turn, the canonical basis of $\mathbb{C}^N$. Hence, for lively quantum walks, the proposed quantum walk corresponds to the unitary matrix $U = S(C \otimes I_N)$, which evolves in time where $C = [c_{ij}] \in U(3)$ and S is the shift operator, which is as follows.

$$\begin{aligned} S = {} & |0\rangle_3 \langle 0|_3 \otimes \sum_{m=0}^{N-1} |m\rangle_N \langle m + 1 (\text{mod } N)|_N \\ & + |1\rangle_3 \langle 1|_3 \otimes \sum_{m=0}^{N-1} |m\rangle_N \langle m - 1 (\text{mod } N)|_N \\ & + |2\rangle_3 \langle 2|_3 \otimes \sum_{m=0}^{N-1} |m + a (\text{mod } N)\rangle_N \langle m|_N \end{aligned} \tag{1}$$

for some liveliness factor $a \leqslant \lfloor \frac{N}{2} \rfloor$, i.e., the walker moves right,left or can jump to another vertex depending on the coin states. When $a = 0$, the walk takes the form of the standard lazy three state quantum walk, i.e., the walker may also stay put instead of jumping off to another vertex.

Hence, the discrete-time evolution of the walk is defined by $|\psi(t)\rangle = U^t |\psi(0)\rangle$ for an initial state $|\psi(0)\rangle \in \mathcal{H}$. Consequently,

$$\begin{aligned} |\psi(t)\rangle &= U^t |\psi(0)\rangle \\ &= \sum_{m=0}^{N-1} \sum_{l \in \{0,1,2\}} \psi(l, m, t) |l\rangle_3 \otimes |m\rangle_N \\ &= \sum_{m=0}^{N-1} |\psi(m, t)\rangle \otimes |m\rangle_N , \end{aligned} \tag{2}$$

where $\sum_{l=0}^{2} \sum_{m=0}^{N-1} |\psi(l, m, t)|^2 = 1$.

2. Three-state quantum walk model on Cay($D_N, \{\mu, \xi\}$)

Similar to lively quantum walk in cycles, the three-state DTQW on Cay($D_N, \{\mu, \xi\}$) is defined on the Hilbert space $\mathcal{H} = \mathcal{H}_C \otimes \mathcal{H}_V$ where $\mathcal{H}_C = \text{span}\{|0\rangle_3, |1\rangle_3, |2\rangle_3\}$ is the coin space and $\mathcal{H}_V$ is the Hilbert space spanned by the vertices of $|(s,r)\rangle \in V$ of Cay($D_N, \{\mu, \xi\}$).

Hence, $\mathcal{H}_V = \text{span}\{|s\rangle_2 |r\rangle_N \,|s \in \{0,1\}, r \in \{0,1,\dots,N-1\}\} \cong \mathbb{C}^2 \otimes \mathbb{C}^N$. Thus the vertex set is given by

$$\{\overbrace{|0\rangle_2 |0\rangle_N, |0\rangle_2 |1\rangle_N, \dots |0\rangle_2 |N-1\rangle_N}^{\text{rotation without reflection}},$$

$$\overbrace{|1\rangle_2 |0\rangle_N, |1\rangle_2 |1\rangle_N, \dots |1\rangle_2 |N-1\rangle_N}^{\text{rotation after reflection}}\},$$

where the first qubit $|.\rangle_2$ represents the reflection qubit such that $\{|s\rangle_2 \,|\, s = 0,1\}$ is the canonical basis of $\mathbb{C}^2$ and $\{|r\rangle_N \,|0 \leqslant r \leqslant N-1\}$ is the canonical basis of $\mathbb{C}^N$. It is evident that the vertices labeled $(0,r)$ are the rth vertices and the vertices labeled $(1,r)$ are the $(N+r)$th vertices, $0 \leqslant r \leqslant N-1$. The proposed quantum walk evolves via the following unitary matrix $U = S(C \otimes I_2 \otimes I_N)$, where $C = [c_{ij}] \in U(3)$ and S is the shift operator defined in the following way. We follow the walk described in Refs. [11,12], i.e., the walker performs one rotation in the direction of the edges of the cycle on which the walker resides if the coin state is $|0\rangle_3$. If the reflection state is $|0\rangle_2$, the walker moves along the inner directed cycle and if the reflection state is $|1\rangle_2$, the walker moves along the outer directed cycle. The walker remains at the same position if the coin state is $|1\rangle_3$, and walker jumps cycles via one reflection if the coin state is $|2\rangle_3$.

Then the shift operator is defined as

$$\begin{aligned} S &= |0\rangle_3 \langle 0|_3 \otimes |0\rangle_2 \langle 0|_2 \otimes \sum_{r=0}^{N-1} |r\rangle_N \langle r-1 (\text{mod } N)|_N \\ &+ |0\rangle_3 \langle 0|_3 \otimes |1\rangle_2 \langle 1|_2 \otimes \sum_{r=0}^{N-1} |r\rangle_N \langle r+1 (\text{mod } N)|_N \\ &+ |1\rangle_3 \langle 1|_3 \otimes |0\rangle_2 \langle 0|_2 \otimes \sum_{r=0}^{N-1} |r\rangle_N \langle r|_N \\ &+ |1\rangle_3 \langle 1|_3 \otimes |1\rangle_2 \langle 1|_2 \otimes \sum_{r=0}^{N-1} |r\rangle_N \langle r|_N \\ &+ |2\rangle_3 \langle 2|_3 \otimes |0\rangle_2 \langle 1|_2 \otimes \sum_{r=0}^{N-1} |r\rangle_N \langle r|_N \\ &+ |2\rangle_3 \langle 2|_3 \otimes |1\rangle_2 \langle 0|_2 \otimes \sum_{r=0}^{N-1} |r\rangle_N \langle r|_N . \end{aligned} \tag{3}$$

The discrete-time evolution of the walk is defined by $|\psi(t)\rangle = U^t |\psi(0)\rangle$ for an initial state $|\psi(0)\rangle \in \mathcal{H}$ where U is a $6N \times 6N$ matrix. Consequently,

$$\begin{aligned} |\psi(t)\rangle &= U^t |\psi(0)\rangle \\ &= \sum_{s=0,1} \sum_{r=0}^{N-1} \sum_{l \in \{0,1,2\}} \psi(l,s,r,t) |l\rangle_3 \otimes |s\rangle_2 \otimes |r\rangle_N, \end{aligned} \tag{4}$$

where $\sum_{l=0}^{2} \sum_{s=0}^{1} \sum_{r=0}^{N-1} |\psi(l,s,r,t)|^2 = 1$.

Remark 1. Note that constructing a qutrit circuit for this walk is challenging since the reflection state is two dimensional, i.e., it represents a qubit. However, we will see later in Sec. III that constructing a circuit by taking the reflection state as a qutrit instead of qubit preserves the walk.

C. Qutrit rotation gates, qutrit X gates and two-qutrit controlled gates

Now, we recall some elementary quantum gates for qutrits such as qutrit rotation gates, qutrit X gates along with the two-qutrit controlled gates, which will play the pivotal role in developing a circuit model of the quantum walks discussed above. Obviously, the qubit rotation gates are given by

$$R_X(\theta) = \begin{bmatrix} \cos\theta & i\sin\theta \\ i\sin\theta & \cos\theta \end{bmatrix}, \quad R_Y(\theta) = \begin{bmatrix} \cos\theta & \sin\theta \\ -\sin\theta & \cos\theta \end{bmatrix},$$
$$R_Z(\theta) = \begin{bmatrix} e^{i\theta} & 0 \\ 0 & e^{-i\theta} \end{bmatrix}, \tag{5}$$

which represent the rotation of a qubit on the Bloch sphere around an angle θ with respect to the X, Y, and Z axes, respectively. Here $i = \sqrt{-1}$.

Now since a qutrit has three dimensions, we use the following elementary qutrit gates, which were first used in Refs. [39,46]. These gates are formed by applying the qubit rotation gates on the subspace of dimension 2 for a qutrit keeping the remaining dimension unchanged. Thus we have the following qutrit rotation gates:

$$R_{X01}(\theta) = \begin{bmatrix} \cos\theta & i\sin\theta & 0 \\ i\sin\theta & \cos\theta & 0 \\ 0 & 0 & 1 \end{bmatrix}, \quad R_{X12}(\theta) = \begin{bmatrix} 1 & 0 & 0 \\ 0 & \cos\theta & i\sin\theta \\ 0 & i\sin\theta & \cos\theta \end{bmatrix}, \quad R_{X02}(\theta) = \begin{bmatrix} \cos\theta & 0 & i\sin\theta \\ 0 & 1 & 0 \\ i\sin\theta & 0 & \cos\theta \end{bmatrix},$$

$$R_{Y01}(\theta) = \begin{bmatrix} \cos\theta & \sin\theta & 0 \\ -\sin\theta & \cos\theta & 0 \\ 0 & 0 & 1 \end{bmatrix}, \quad R_{Y12}(\theta) = \begin{bmatrix} 1 & 0 & 0 \\ 0 & \cos\theta & \sin\theta \\ 0 & -\sin\theta & \cos\theta \end{bmatrix}, \quad R_{Y02}(\theta) = \begin{bmatrix} \cos\theta & 0 & \sin\theta \\ 0 & 1 & 0 \\ -\sin\theta & 0 & \cos\theta \end{bmatrix}$$

$$R_{Z01}(\theta) = \begin{bmatrix} e^{i\theta} & 0 & 0 \\ 0 & e^{-i\theta} & 0 \\ 0 & 0 & 1 \end{bmatrix}, \quad R_{Z12}(\theta) = \begin{bmatrix} 1 & 0 & 0 \\ 0 & e^{i\theta} & 0 \\ 0 & 0 & e^{-i\theta} \end{bmatrix}, \quad R_{Z02}(\theta) = \begin{bmatrix} e^{i\theta} & 0 & 0 \\ 0 & 1 & 0 \\ 0 & 0 & e^{-i\theta} \end{bmatrix}. \tag{6}$$

Thus if p, q, k denote the three dimensions of a qubit then $R_{F\,pq}(\theta)$ denotes the F qubit (subspace generated by p, q) rotation of the qutrit keeping the dimension k fixed. We also use the following gate in sequel:

$$S(\theta) = \begin{bmatrix} e^{i\theta} & 0 & 0 \\ 0 & e^{i\theta} & 0 \\ 0 & 0 & e^{i\theta} \end{bmatrix}. \tag{7}$$

We also recall the following single-qutrit gates considered in Ref. [33] as follows:

$$X_{0,1} = \begin{bmatrix} 0 & 1 & 0 \\ 1 & 0 & 0 \\ 0 & 0 & 1 \end{bmatrix}, \quad X_{1,2} = \begin{bmatrix} 1 & 0 & 0 \\ 0 & 0 & 1 \\ 0 & 1 & 0 \end{bmatrix}, \tag{8}$$

$$X_{0,2} = \begin{bmatrix} 0 & 0 & 1 \\ 0 & 1 & 0 \\ 1 & 0 & 0 \end{bmatrix}, \quad X_{+1} = \begin{bmatrix} 0 & 0 & 1 \\ 1 & 0 & 0 \\ 0 & 1 & 0 \end{bmatrix},$$

$$X_{+2} = \begin{bmatrix} 0 & 1 & 0 \\ 0 & 0 & 1 \\ 1 & 0 & 0 \end{bmatrix}.$$

Obviously, $X_{p,q}$ gate maps $|p\rangle_3$ ($|q\rangle_3$) to $|q\rangle_3$ ($|p\rangle_3$) where for $p, q \in \{0, 1, 2\}$ and X_{+a} gate is a linear transformation from $|p\rangle_3$ to $|a + p \bmod 3\rangle_3$. We will call these single-qutrit gates as qutrit-X gates where $X \in \{X_{0,1}, X_{1,2}, X_{0,2}, X_{+1}, X_{+2}\}$.

Finally, we discuss two-qutrit controlled-X gates represented by a quantum circuit given by

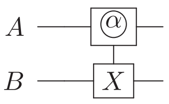

(9)

Obviously, this gate applies one-qutrit X gate on the target (second) qutrit when the control (first) qutrit is $a \in \{0, 1, 2\}$. When $a = 2$, such a gate is called Muthukrishnan-Stroud gate [47]. It is also of note that the circuit

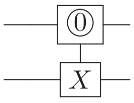

(10)

is equivalent to

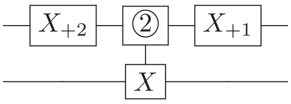

(11)

Similarly, the circuit

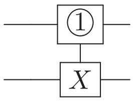

(12)

is equivalent to

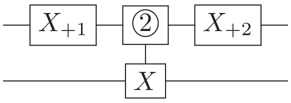

(13)

We denote a n-qutrit gate, also known as n-qutrit controlled-U gate where U is a $(n-1)$-qutrit gate as follows:

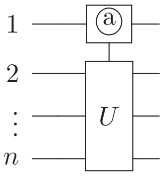

(14)

Another gate we will introduce in this work is the qudit SWAP gate, i.e., given $0 \leqslant a \leqslant b \leqslant d-1$, $|a\rangle_d\, |b\rangle_d \underbrace{\rightarrow}_{SWAP^{(d)}_{a,b}} |b\rangle_d\, |a\rangle_d$. The $SWAP^{(d)}_{a,b}$ is denoted by the following circuit:

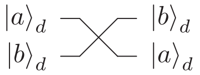

(15)

For $d = 3$, we get the qutrit version of the SWAP gate. It is of note that the $SWAP^{(d)}_{a,b}$ gate can be constructed using three controlled qudit-X gates in the following way,

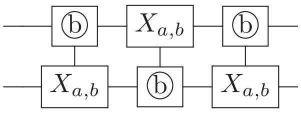

(16)

where $X_{a,b}$ gate maps $|a\rangle_d$ to $|b\rangle_d$ and $|b\rangle_d$ to $|a\rangle_d$.

III. QUTRIT CIRCUIT MODELS FOR THREE-STATE QUANTUM WALKS

It is of note that, the coin operator in a three-state quantum walk or a lively quantum walk is a single-qutrit gate. Hence, it is a perceptible goal to provide a qutrit circuit model in order to realize the three-state DTQWs defined in Sec. II B on $\mathrm{Cay}(D_N, \{\mu, \xi\})$ and $\mathrm{Cay}(\mathbb{Z}_N, \{1, -1\})$, where $3^{n-1} < N \leqslant 3^n$ for some positive integer n. In this section, we will construct qutrit quantum circuit for the said quantum walks using single-qutrit rotation gates and qutrit controlled-X gates or Muthukrishnan-Stroud gate (M-S gate). Our circuit construction is similar to the model proposed for two-state DTQWs on a cycle using Hadamard coins in Ref. [32].

First we provide a theorem that deals with decomposing generic single-qutrit gate into single-qutrit rotation gates in the following section. A similar technique is used in Ref. [48] and a decomposition approach using Cartan algebra is carried in Ref. [39].

A. Decomposition of generic qutrit gates into qutrit-rotation gates

It is well known that for a vector $\begin{bmatrix} a \\ b \end{bmatrix} \in \mathbb{C}^2$, there exists a 2×2 special unitary matrix $\begin{bmatrix} \bar{a} & \bar{b} \\ -b & a \end{bmatrix}$ such that $\frac{1}{\sqrt{|a|^2+|b^2|}} \begin{bmatrix} \bar{a} & \bar{b} \\ -b & a \end{bmatrix} \begin{bmatrix} a \\ b \end{bmatrix} = \begin{bmatrix} \sqrt{|a|^2 + |b|^2} \\ 0 \end{bmatrix}$.

It is also obvious that any 3×3 unitary matrix is a single-qutrit gate. Let the matrix be $C = \begin{bmatrix} c_{11} & c_{12} & c_{13} \\ c_{21} & c_{22} & c_{23} \\ c_{31} & c_{32} & c_{33} \end{bmatrix} \in \mathrm{SU}(3)$ such that each c_{ij} is of the form $r_{ij} e^{-i\alpha_{ij}}$ where $r_{ij} \geqslant 0$ and $\alpha_{ij} \in \mathbb{R}$. Hence, in this section, we provide a decomposition of generic unitary matrix, i.e., a single-qutrit gate into product of rotation gates. We state the following theorem.

Theorem 1. Any 3×3 special unitary matrix $U = [u_{ij}]_{3\times 3}$ has the following parametric representation:

$$\begin{aligned}
u_{11} &= \cos\theta_1 \cos\theta_2 e^{-i\phi_1}\\
u_{12} &= -\sin\theta_1 \sin\theta_3 e^{i(\psi_1-\psi_3)} - \cos\theta_1 \sin\theta_2 \cos\theta_3 e^{i(\psi_2-\phi_1-\phi_3)}\\
u_{13} &= -\sin\theta_1 \cos\theta_3 e^{i(\phi_3+\psi_1)} + \cos\theta_1 \sin\theta_2 \sin\theta_3 e^{i(\psi_2-\phi_1+\psi_3)}\\
u_{21} &= \sin\theta_2 e^{-i\psi_2}\\
u_{22} &= \cos\theta_2 \cos\theta_3 e^{-i\phi_3}\\
u_{23} &= \cos\theta_2 \sin\theta_3 e^{-i(\psi_3-\pi)}\\
u_{31} &= \sin\theta_1 \cos\theta_2 e^{-i\psi_1}\\
u_{32} &= \cos\theta_1 \sin\theta_3 e^{i(\phi_1-\psi_3)} - \sin\theta_1 \sin\theta_2 \cos\theta_3 e^{i(\psi_2-\psi_1-\phi_3)}\\
u_{33} &= \cos\theta_1 \cos\theta_3 e^{i(\phi_1+\phi_3)} + \sin\theta_1 \sin\theta_2 \sin\theta_3 e^{i(-\psi_1+\psi_2+\psi_3)}
\end{aligned}$$

where $\theta_1, \theta_2, \theta_3, \phi_1, \phi_3, \psi_1, \psi_2, \psi_3 \in \mathbb{R}$. Besides, U has the following factorization through qutrit-rotation gates:

$$\begin{aligned}
U = {}& R_{Z02}\left(\frac{-\phi_1+\psi_1}{2}\right) R_{Y02}(-\theta_1) R_{Z02}\left(\frac{-\phi_1-\psi_1}{2}\right)\\
& R_{Z01}\left(\frac{\psi_2}{2}\right) R_{Y01}(-\theta_2) R_{Z01}\left(\frac{-\psi_2}{2}\right)\\
& R_{Z12}\left(\frac{-\phi_3+\psi_3}{2}\right) R_{Y12}(-\theta_3) R_{Z12}\left(\frac{-\phi_3-\psi_3}{2}\right).
\end{aligned}$$

Proof. See the discussion in Appendix A.

Remark 2.

(1) The Theorem 1 can be considered as qutrit analog of the qubit ZYZ decomposition.

(2) It is to be noted that the matrix U in Theorem 1, requires eight parameters, which is precisely the dimension of the manifold SU(3).

(3) Given any matrix from SU(3), the nine equations are easily solvable. For example, let us take $V = [v_{ij}]_{3\times 3} \in$ SU(3). Then through some computation, we obtain

$$\begin{aligned}
&\theta_2 = \arcsin|v_{21}|,\ \psi_2 = \arctan\arg(v_{21})\\
&\theta_1 = \arccos\frac{|v_{11}|}{\cos\theta_2},\ \text{where } \theta_2 \neq \frac{\pi}{2}\\
&\phi_1 = -\arctan\arg(v_{11}),\ \psi_1 = -\arctan\arg(v_{31})\\
&\theta_3 = \arccos\frac{|v_{22}|}{\cos\theta_2},\ \text{where } \theta_2 \neq \frac{\pi}{2}\\
&\phi_3 = -\arctan\arg(v_{22}),\ \psi_3 = -\arctan\arg(v_{23}) + \pi.
\end{aligned}$$

We will take $\psi_3 = 0, \theta_1 = \frac{\pi}{2} = \theta_3$, when $\theta_2 = \frac{\pi}{2}$.

(4) Further, any 3×3 unitary matrix can be written as $e^{i\alpha}U$ for some real α where $U \in$ SU(3). Thus any unitary matrix has a similar decomposition.

(5) Given a 3×3 diagonal matrix $D = \text{diag}(e^{i\alpha}, e^{i\beta}, e^{i\zeta}) \in U(3), \alpha, \beta, \zeta \in \mathbb{R}$. Then

$$\begin{aligned}
D = {}& \exp\left(\frac{\alpha+\beta+\zeta}{3} I\right) R_{Z01}\left(\frac{2\alpha-\beta-\zeta}{3}\right)\\
& R_{Z12}\left(\frac{\alpha+\beta-2\zeta}{3}\right).
\end{aligned}$$

It is also of note that a 3×3 diagonal unitary matrix of the form $\tilde{D} = \text{diag}(e^{i\alpha}, e^{i\beta}, e^{-i(\alpha+\beta)}) \in \text{SU}(3), \alpha, \beta \in \mathbb{R}$ can be decomposed as

$$\begin{aligned}
\tilde{D} &= R_{Z01}(\alpha) R_{Z12}(\alpha+\beta) = R_{Z02}(\alpha) R_{Z12}(\beta)\\
&= R_{Z02}(\alpha+\beta) R_{Z01}(-\beta).
\end{aligned}$$

B. Qutrit circuit model for DTQW on Cay(D_N, {μ, ξ})

Recall that the vertices of Cay$(D_N, \{\mu, \xi\})$ are labeled as $(s, r), s \in \{0, 1\}, r \in \{0, 1 \dots, N-1\}$ where s denotes the reflection and r denotes rotation. Thus the position space is given by the Hilbert space $\mathcal{H}_V = \text{span}\{|s\rangle_2 |r\rangle_N : s \in \{0, 1\}, r \in \{0, 1, \dots, N-1\}\} \cong \mathbb{C}^2 \otimes \mathbb{C}^N$. Now in order to incorporate this labeling into the proposed qutrit circuit model, we consider the quantum states corresponding to the vertex set as $\{|s\rangle_3 |r_n\rangle_3 |r_{n-1}\rangle_3 \dots |r_1\rangle_3 : s \in \{0, 1\}, r_j \in \{0, 1, 2\}, j \in \{1, 2, \dots, n-1\}\}$ where the ternary representation of r is given by $r = \sum_{j=1}^{n} r_j 3^{j-1}$, i.e., $|r\rangle_N = |r_n\rangle_3 |r_{n-1}\rangle_3 \dots |r_1\rangle_3$. It is also of note that the reflection state $|s\rangle_2$ belongs to $\mathbb{C}^2$, which we consider as a qutrit, i.e., $|s\rangle_3$. Hence, $|s\rangle_3 \in \{|0\rangle_3, |1\rangle_3, |2\rangle_3\}$, the canonical basis sates of $\mathbb{C}^3$. Thus, from our construction, we label the rth vertex of the inner cycle of Cay$(D_N, \{\mu, \xi\})$ labeled by $(0, r)$ as $|0\rangle_3 |r_n\rangle_3 |r_{n-1}\rangle_3 \dots |r_1\rangle_3$ where $0 \leqslant r_j \leqslant 2$; and the state $|1\rangle_3 |r_n\rangle_3 |r_{n-1}\rangle_3 \dots |r_1\rangle_3$ represents the $(N+r)$th vertex labeled by $(1, r)$, i.e., the rth vertex in the outer cycle of Cay$(D_N, \{\mu, \xi\})$. Because of such qutrit circuit representation of vertices, it is evident that $n+1$ qutrits are required to describe the position space, in which the first qutrit represents the reflection state and the rest n qutrits for the reflection state. We will use another qutrit for the quantum coin state from $\mathbb{C}^3$. Hence, for the quantum circuit model of the quantum walk, $n+2$ qutrits are required, i.e., the unitary matrix corresponding to the qutrit quantum circuit is of order 3^{n+2}.

Moreover, the circuit should be constructed in such a way that the input states of the form $|c\rangle_3 |2\rangle_3 |r_n\rangle_3 |r_{n-1}\rangle_3 \dots |r_1\rangle_3$ remain invariant where $|c\rangle_3 \in \mathcal{H}_C$ denotes the coin state such that $c \in \{0, 1, 2\}, r_j \in \{0, 1, 2\}, j \in \{1, 2, \dots, n\}$. By constructing the circuit in such a way, we will prove that the quantum circuit thus formed does not impede on the structure of the walk. First, we construct the following qutrit quantum gates using a similar approach used in Ref. [32].

INCREMENT:

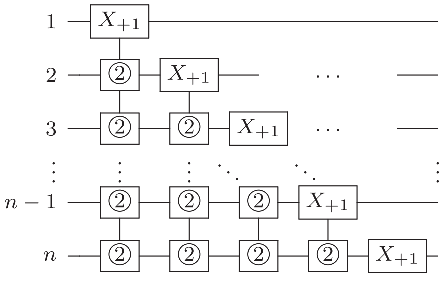

(17)

and

DECREMENT:

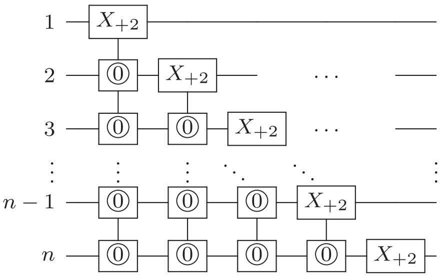

(18)

Clearly, these gates comprise of multicontrolled qutrit gates. Each string of qutrits representing the rotation state of the vertex after passing through increment or decrement will always give us the immediate adjacent rotation state, i.e.,

$$|r_n\rangle_3\,|r_{n-1}\rangle_3\dots|r_1\rangle_3 \underset{\text{increment}}{\overbrace{\rightarrow}} |r'_n\rangle_3\,|r'_{n-1}\rangle_3\dots|r_1\rangle_3$$

$$|r_n\rangle_3\,|r_{n-1}\rangle_3\dots|r_1\rangle_3 \underbrace{\rightarrow}_{\text{decrement}} |\tilde{r}_n\rangle_3\,|\tilde{r}_{n-1}\rangle_3\dots|\tilde{r}_1\rangle_3$$

where $\sum_{j=1}^{n} r'_j 3^{j-1} = (r+1) \mod N$ and $\sum_{j=1}^{n} \tilde{r}_j 3^{j-1} = (r-1) \mod N$. It is also evident that when the coin state is $|0\rangle_3$ and reflection state is $|0\rangle_3$ then using the INCREMENT gates on the rotation states, the state $|0\rangle_3\,|0\rangle_3\,|r_n\rangle_3\,|r_{n-1}\rangle_3\dots|r_1\rangle_3$ is mapped to $|0\rangle_3\,|0\rangle_3\,|r'_n\rangle_3\,|r'_{n-1}\rangle_3\dots|r'_1\rangle_3$. Similarly, when the coin state is $|0\rangle_3$ and reflection state is $|1\rangle_3$, then using the DECREMENT gates on the rotation states, the state $|0\rangle_3\,|1\rangle_3\,|r_n\rangle_3\,|r_{n-1}\rangle_3\dots|r_1\rangle_3$ is mapped to $|0\rangle_3\,|1\rangle_3\,|\tilde{r}_n\rangle_3\,|\tilde{r}_{n-1}\rangle_3\dots|\tilde{r}_1\rangle_3$. Besides, the INCREMENT and DECREMENT gates also maintain a periodic condition of the walk, which means $|0\rangle_3\,|0\rangle_3\dots|0\rangle_3$ and $|2\rangle_3\,|2\rangle_3\dots|2\rangle_3$ are adjacent rotation states. Hence these gates map rth [$(N+r)$th] vertex to $(r\pm 1)$th [$(N+r\pm 1)$th] vertex.

Now, using all previous circuits discuss above, we present the circuit model for three-state quantum walks on Cayley graph of dihedral group $\mathrm{Cay}(D_N, \{\mu, \xi\})$ where $N = 3^n$ as follows:

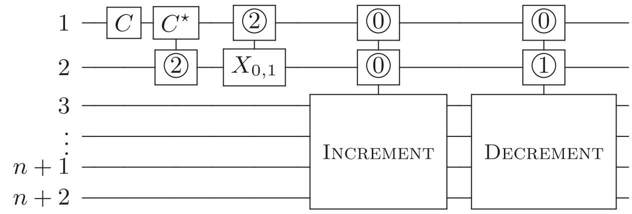

(19)

where C and $C^\star$ are the coin operator and its inverse, respectively.

From our proposed circuit, we observe the following.

(1) Let $N = 27$ and the walker starts with the state $|0\rangle_3^{\otimes 5}$ at $t = 0$. Let the coin $C = (c_{ij})_{3\times 3}$. Then at $t = 1$, the walker has the state $|\psi(1)\rangle = c_{11}\,|0\rangle_3\,|0\rangle_3\,|001\rangle_3 + c_{21}\,|1\rangle_3\,|0\rangle_3\,|000\rangle_3 + c_{31}\,|2\rangle_3\,|1\rangle_3\,|000\rangle_3$. This is due to the fact that $C\,|0\rangle_3 = c_{11}\,|0\rangle_3 + c_{21}\,|1\rangle_3 + c_{31}\,|2\rangle_3$. Now since the second qutrit is not $|2\rangle_3$, it remains unaffected through the second gate in the circuit and then the $X_{0,1}$ gate applies when the first qutrit is $|2\rangle_3$. The final two gates act as increment or decrement operators when the first two qutrits of the state of the walker are $|0\rangle_3\,|0\rangle_3$ and $|0\rangle\,|1\rangle_3$, respectively, and we get our result. Similarly for $t = 2$, we get the following state:

$$\begin{aligned}|\psi(2)\rangle = {} & c_{11}^2\,|0\rangle_3\,|0\rangle_3\,|002\rangle_3 + c_{11}c_{21}\,|1\rangle_3\,|0\rangle_3\,|001\rangle_3 \\ & + c_{11}c_{31}\,|2\rangle_3\,|1\rangle_3\,|001\rangle_3 + c_{12}c_{21}\,|0\rangle_3\,|0\rangle_3\,|001\rangle_3 \\ & + c_{22}c_{21}\,|1\rangle_3\,|0\rangle_3\,|000\rangle_3 + c_{32}c_{21}\,|2\rangle_3\,|1\rangle_3\,|000\rangle_3 \\ & + c_{31}c_{13}\,|0\rangle_3\,|1\rangle_3\,|222\rangle_3 + c_{31}c_{23}\,|1\rangle_3\,|1\rangle_3\,|000\rangle_3 \\ & + c_{31}c_{33}\,|2\rangle_3\,|0\rangle_3\,|000\rangle_3\,.\end{aligned}$$

The probability of finding the walker at the starting point (0,0), i.e., $|0\rangle_3\,|000\rangle_3$ at $t = 2$ is $|c_{22}c_{21}|^2 + |c_{31}c_{33}|^2$.

When $N = 25$, for $t = 2$, the state becomes

$$\begin{aligned}|\psi(2)\rangle = {} & c_{11}^2\,|0\rangle_3\,|0\rangle_3\,|002\rangle_3 + c_{11}c_{21}\,|1\rangle_3\,|0\rangle_3\,|001\rangle_3 \\ & + c_{11}c_{31}\,|2\rangle_3\,|1\rangle_3\,|001\rangle_3 + c_{12}c_{21}\,|0\rangle_3\,|0\rangle_3\,|001\rangle_3 \\ & + c_{22}c_{21}\,|1\rangle_3\,|0\rangle_3\,|000\rangle_3 + c_{32}c_{21}\,|2\rangle_3\,|1\rangle_3\,|000\rangle_3 \\ & + c_{31}c_{13}\,|0\rangle_3\,|1\rangle_3\,|221\rangle_3 + c_{31}c_{23}\,|1\rangle_3\,|1\rangle_3\,|000\rangle_3 \\ & + c_{31}c_{33}\,|2\rangle_3\,|0\rangle_3\,|000\rangle_3\,.\end{aligned}$$

It is easy to see that for $t = 1$ and $t = 2$, the final state becomes a linear combination of three and nine quantum states, respectively, and the walker passes over three and six distinct vertices, respectively.

(2) The input state $|l\rangle_3\,|2\rangle_3\,|r_n\rangle_3\dots|r_1\rangle_3$ is invariant for all $l \in \{0, 1, 2\}$, $r_j \in \{0, 1, 2\}$, $j \in \{1, \dots, n\}$.

(3) The quantum circuit is scalable, i.e., using the circuit for DTQW on $\mathrm{Cay}(D_{3^n}, \{\mu, \xi\})$, one can construct the circuit for DTQW on $\mathrm{Cay}(D_{3^{n+1}}, \{1, -1\})$, by addition of multicontrolled qutrit-X gates to construct INCREMENT and DECREMENT gates.

The quantum circuit proposed so far can also be modified for $\mathrm{Cay}(D_N, \{\mu, \xi\})$, $3^{n-1} < N < 3^n$. The main idea is to incorporate necessary qutrit controlled gates in between the INCREMENT and DECREMENT gates so that the periodic conditions are suitably modified. Let, $N = k < 3^n$ and hence, $k = \sum_{j=1}^{n} 3^{j-1}k_j$ where $k_j \in \{0, 1, 2\}$, $0 \leqslant j \leqslant n$ and not all k_j's are equal to 2. Then we assign necessary multicontrolled qutrit-X gates in order to modify the periodic conditions so that the $|s\rangle_3\,|k_n\rangle_3\dots|k_1\rangle_3$ and $|s\rangle_3\,|0\rangle_3\dots|0\rangle_3$ are adjacent vertices for $s \in \{0, 1\}$. Let us consider $|k'_n\rangle_3\dots|k'_1\rangle_3$ such that $|k'_n\rangle_3\dots|k'_1\rangle_3$ and $|k_n\rangle_3\dots|k_1\rangle_3$ differ in exactly one qutrit. We call these vertices as Hamming-1 vertices. Hence, the main idea is to find suitable set of multicontrolled qutrit-X gates such that we can construct a mapping between the vertices in the following way,

$$\begin{array}{ccc} |0\rangle_3\,|k_n\rangle_3\dots|k_1\rangle_3 & \mapsto & |0\rangle_3\,|k'_n\rangle_3\dots|k'_1\rangle_3 \\ & \underbrace{\dots\mapsto}_{\text{Hamming-1 vertices}} & |0\rangle_3\,|2\rangle_3\dots|2\rangle_3 \\ & \mapsto & |0\rangle_3\,|0\rangle_3\dots|0\rangle_3 \\ \hline |1\rangle_3\,|0\rangle_3\dots|0\rangle_3 & \mapsto & |1\rangle_3\,|2\rangle_3\dots|2\rangle_3 \\ & \underbrace{\dots\mapsto}_{\text{Hamming-1 vertices}} & |1\rangle_3\,|k'_n\rangle_3\dots|k'_1\rangle_3 \\ & \mapsto & |1\rangle_3\,|k_n\rangle_3\dots|k_1\rangle_3\,. \end{array}$$

The mapping from one state $|k_n\rangle_3\dots|k_1\rangle_3$ to another state $|0\rangle_3\dots|0\rangle_3$ by creating a sequence of Hamming-1 vertices, is similar to the construction of qubit circuits that maps one state to another through multicontrolled CNOT gates using Gray codes [49].

For any N, the basic idea is to incorporate a multicontrolled qutrit-X gate with the target qutrit located at the single position where the two adjacent Hamming-1 vertices differ, and then undoing the process. To be more descriptive, suppose we are given a starting state $a = |a_n\rangle_3 \ldots |a_1\rangle_3$ and ending state $b = |b_n\rangle_3 \ldots |b_1\rangle_3$ and our aim is to construct a quantum gate that maps a to b and b to a. Then we want to find a sequence of Hamming-1 vertices such that

$$a \mapsto a^{(1)}, \underbrace{\ldots\ldots}_{\text{Hamming-1 vertices}}, a^{(n-1)} \mapsto a^{(n)} = b.$$

Thus, first we will find a multicontrolled qutrit-X gate that swaps a and $a^{(1)}$. Suppose a and $a^{(1)}$ differ at the ith digit. Then a multicontrolled X gate can be used to flip the qutrit on the ith position. The multicontrolled qutrit-X gate is constructed keeping in mind the values of the other qutrits being same to those in both a and $a^{(1)}$. This process can be repeated for $a^{(1)}$ and $a^{(2)}$ until a multicontrolled qutrit-X gate is obtained that maps $a^{(n-1)}$ to b and vice versa. Hence, using this construction, one can map from a to b. In order to complete the circuit however, the circuit must also map from b to a. A similar construction can be designed as follows. Suppose b and $a^{(n-1)}$ differ in the jth qutrit. Then apply a multicontrolled qutrit-X gate with the jth qutrit as target and the gate being conditional on the other qutrits having the same values as in both b and $a^{(n-1)}$. Hence, continuing this way, a map can be constructed in order to obtain the sequence

$$b \mapsto a^{(n-1)}, \underbrace{\ldots\ldots}_{\text{Hamming-1 vertices}}, a^{(1)} \mapsto a.$$

Let us look at an example. Consider three-state DTQW on $\text{Cay}(D_{25}, \{\mu, \xi\})$. In this case $N = 25$, which is less than $27 = 3^3$. Hence in this case, the last vertex of both directed cycles in the graph is represented by $|s\rangle_3\,|2\rangle_3\,|2\rangle_3\,|0\rangle_3$, $s \in \{0, 1\}$. Hence, we will incorporate multicontrolled qutrit gates comprising of generalized multicontrolled qutrit-X gates in between the INCREMENT and DECREMENT gates such that $|s\rangle_3\,|0\rangle_3\,|0\rangle_3\,|0\rangle_3$ and $|s\rangle_3\,|2\rangle_3\,|2\rangle_3\,|0\rangle_3$ are adjacent vertices and the input states $|l\rangle_3\,|s\rangle_3\,|2\rangle_3\,|2\rangle_3\,|2\rangle_3$ and $|c\rangle_3\,|s\rangle_3\,|2\rangle_3\,|2\rangle_3\,|1\rangle_3$ remains invariant in the circuit where $|c\rangle_3$ is the coin state such that $c \in \{0, 1, 2\}$. Thus we construct the following two unitaries.

INSTOP:

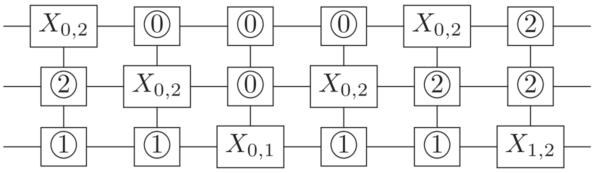

(20)

and

DESTOP:

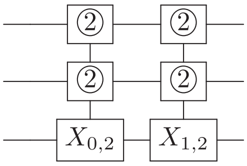

(21)

Using the gates above, the circuit for the walk on $\text{Cay}(D_{25}, \{\mu, \xi\})$ is given by

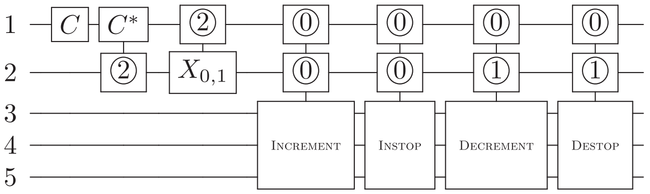

(22)

Now, we will prove that constructing quantum circuits with reflection states as qutrits does not affect the structure of the walk.

Theorem 2. Let $U_{\text{Cay}(D_N)} \in \mathbb{C}^{6N\times 6N}$, $3^{n-1} \leqslant N \leqslant 3^n$ be the unitary matrix corresponding to the three-state DTQW on $\text{Cay}(D_N, \{\mu, \xi\})$ obtained theoretically as described in Sec. II B 2. Also, let $U_{\text{circ}} \in \mathbb{C}^{3^{n+2}\times 3^{n+2}}$ be the unitary matrix corresponding to the qutrit circuit for the three-state DTQW $\text{Cay}(D_N, \{\mu, \xi\})$. Then there exists a permutation matrix P such that

$$U_{\text{circ}} = P\left[\begin{array}{c|c} U_{\text{Cay}(D_N)} & 0 \\ \hline 0 & I_{(3^{n+2}-6N)} \end{array}\right]P^T.$$

Proof. See Appendix B. ■.

Hence, we have successfully provided a qutrit quantum circuit for three-state discrete-time quantum walk on $\text{Cay}(D_N, \{\mu, \xi\})$. In the next section, we will provide somewhat similar circuit construction for three-state lively quantum walks on cycle graphs.

C. Qutrit circuit model for three-state lively DTQWs on $\text{Cay}(\mathbb{Z}_N, \{1, -1\})$

We now propose a qutrit quantum circuit model for the lively DTQW on cycle graphs [9]. We recall that the walker moves to the left if the coin state $|0\rangle_3$ and walker moves to the right if the coin state is $|1\rangle_3$ and jumps to vertex at distance $a(\mod N)$ if the coin state is $|2\rangle_3$ where $0 < a \leqslant \lfloor \frac{N}{2} \rfloor$ is the liveliness parameter. For $a = 0$, it is obvious that the walk becomes a standard three-state lazy quantum walk [9] on cycles. For further analysis of the walk, see Refs. [9,41].

Similar to the previous model, in our circuit model, we see that for the cycle of length $3^{n-1} < N \leqslant 3^n$, we require total $n + 1$ qutrits. The first qutrit is required for the coin states and the rest n qutrits are required for the vertices in order to represent the position states. We first construct the simple model of three-state lively quantum walks on cycles where the liveliness parameter is taken to be 0, i.e., the standard three-state lazy quantum walk. The circuit for three-state lazy DTQW on cycle of length 3^n is as follows:

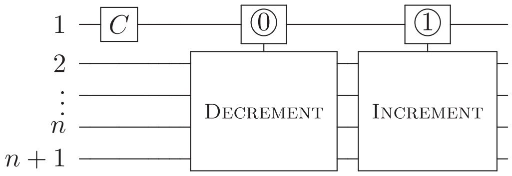

(23)

The observations obtained from the above circuit are as follows.

(1) The walker has a nonzero probability of being found at all vertices of the cycle after N time steps.

(2) The quantum circuit is again scalable.

Similarly, when $3^{n-1} < N < 3^n$ we use multicontrolled qutrit X gates in between. For example, let us look at a walk with 25 vertices. Then we take the circuit

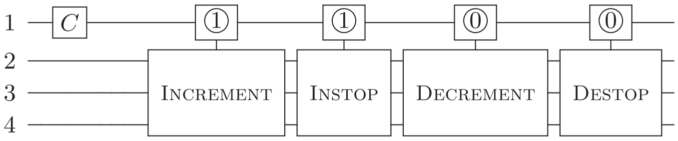

(24)

For lively quantum walk on cycles with nonzero liveliness operator $a \leqslant \lfloor \frac{N}{2} \rfloor$ and $N = 3^n$, the circuit needs to be modified slightly in the following manner. Define a new repeated circuit RC(a) as

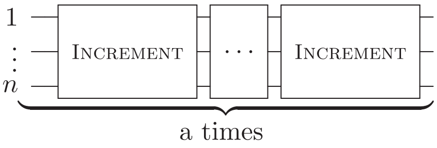

(25)

Hence, the circuit for three-state lazy DTQWs on cycle of length 3^n is as follows.

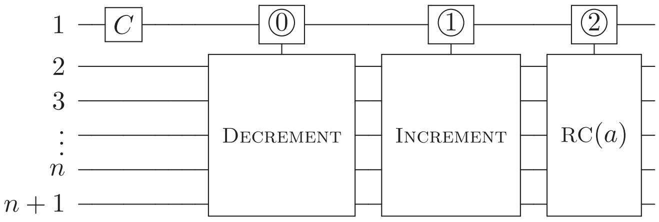

(26)

Similarly, when $3^{n-1} < N < 3^n$, then one can add the gates INSTOP and DESTOP in the circuit to modify the periodic condition.

Remark 3. Note from our circuit construction that the coin operators C and $C^\star$ can be implemented though the elementary qutrit gates due to Theorem 1 (special unitary matrix) and a global phase. However, the implementation of multicontrolled qutrit gates used to construct INCREMENT, DECREMENT, INSTOP, and DESTOP through elementary qutrit gates need further investigation. These circuits can also be viewed as n-qutrit Toffoli gates. In Sec. IV, we provide construction of qutrit circuits for block diagonal unitary matrices for 3 × 3 diagonal blocks and any n-qutrit Toffoli gate is a special case.

IV. SCALABLE QUTRIT CIRCUIT IMPLEMENTATION OF 3 × 3 BLOCK DIAGONAL UNITARY MATRICES

The quantum circuit models as proposed above utilize multicontrolled qutrit-X gates of the following form:

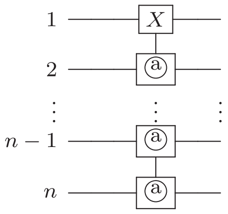

(27)

where $a \in \{0, 1, 2\}$. In this section, we develop a quantum circuit model of its implementation through single-qutrit rotation gates and controlled qutrit-X gates.

First, we note that the matrix representation of the circuit

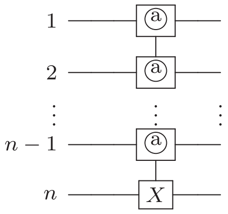

(28)

is a block diagonal special unitary matrix. In what follows, we construct an ancilla-free quantum circuit for n-qutrit block-diagonal special unitary matrices having 3 × 3 special unitary blocks using M-S gates and single-qutrit rotation gates.

We emphasize that the obtained circuit is scalable, i.e., we can construct circuit for $(n+1)$-qutrit block-diagonal special unitary using circuits from n-qutrit block-diagonal special unitary. The construction is also exact and the process follows similar to work done in Ref. [12]. It is also of note that since any unitary matrix U can always be expressed as $e^{i\alpha}V$ for some $\alpha \in \mathbb{R}$ and V is a special unitary matrix, i.e., any unitary matrix is a special unitary matrix multiplied by a global phase, hence, we restrict our construction to special unitary matrices only. Using the construction of block diagonal unitary matrices and in turn, the circuit in Eq. (28), we also provide a circuit construction for the qutrit gate in Eq. (27).

Definition 1. For n-qutrit systems, a multicontrolled rotation gate is defined as

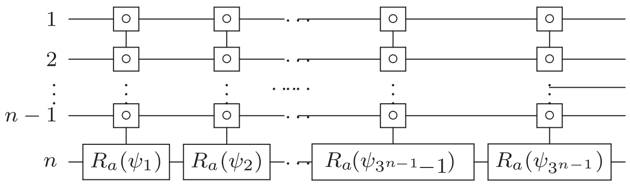

(29)

$\psi_j \in \mathbb{R}, 1 \leqslant j \leqslant 3^{n-1}$ and

$$a \in \{X01, X02, X12, Y01, Y02, Y12, Z01, Z02, Z12\}.$$

Then the unitary matrix corresponding to the above circuit is given by

$$F_n(R_a(\psi_1, \psi_2, \dots, \psi_{3^{n-1}})) = \left[\begin{array}{c|c|c} R_a(\psi_1) & 0 & 0 \\ \hline 0 & \ddots & 0 \\ \hline 0 & 0 & R_a(\psi_{3^{n-1}}) \end{array}\right],$$

which is a block diagonal matrices with 3×3 rotation blocks.

In short, we denote the circuit in Definition 1 as

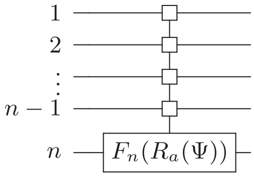

(30)

such that $\Psi = (\psi_1, \dots, \psi_{3^{n-1}})$.

In order to demonstrate the scalability of such multicontrolled gates, win the following we construct $(n+1)$-qutrit multicontrolled gates that consists of n-qutrit multicontrolled rotation gates and some additional two-qutrit control gates. It is to be noted that similar construction has been done in Ref. [39], however, in this work, we provide a more general construction of generalized Toffoli gates mentioned in Eq. (27) using the construction of multicontrolled qutrit-X gates.

First, consider the following circuits. with $, \Phi = (\phi_1, \dots, \phi_{3^{n-2}}), \Theta = (\theta_1, \dots, \theta_{3^{n-2}}), \Gamma = (\gamma_1, \dots, \gamma_{3^{n-2}})$:

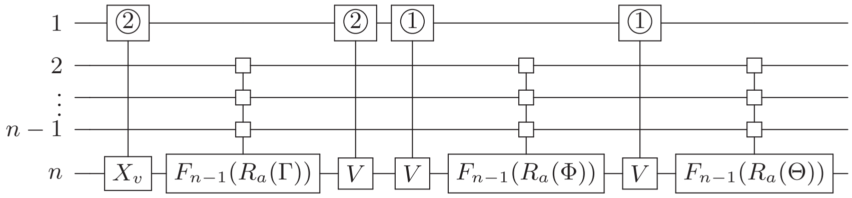

(31)

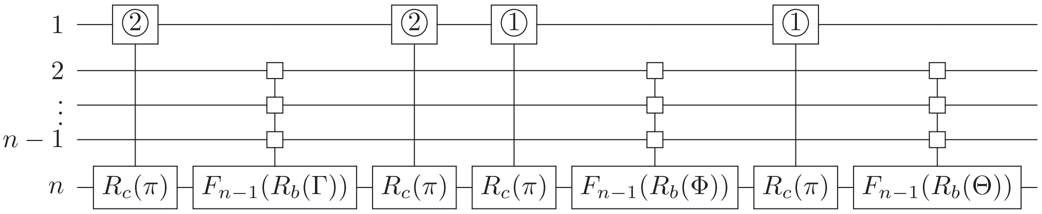

(32)

where

$$\psi_k = \begin{cases} \theta_j + \phi_j + \gamma_j & \text{where } 1 \leqslant j \leqslant 3^{n-2}, k = j \\ \theta_j - \phi_j + \gamma_j & \text{where } 1 \leqslant j \leqslant 3^{n-2}, k = j + 3^{n-2} \\ \theta_j + \phi_j - \gamma_j & \text{where } 1 \leqslant j \leqslant 3^{n-2}, k = j + 2 \cdot 3^{n-2}. \end{cases}$$

Then we have the following lemma.

Lemma 1. The following statements hold true:

(1) The quantum circuits in Eq. (30) and Eq. (31) are equivalent when any of the cases hold:
$R_a \in \{R_{Y01}, R_{Z01}\}$ and $V = X_{0,1}$ or ,
$\{R_a \in \{R_{Y12}, R_{Z12}\}$ and $V = X_{1,2}$ or ,
$R_a \in \{R_{Y02}, R_{Z02}\}$ and $V = X_{0,2}$.

(2) The quantum circuits in Eq. (30) and Eq. (32) are equivalent when any of the cases hold:
$R_a = R_{X02}$ and $R_b = R_{Z12}, R_c = R_{X02}$, or ,
$\{R_a = R_{X01}$ and $R_b = R_{Z12}, R_c = R_{X01}$, or ,
$R_a = R_{X12}$ and $R_b = R_{Z02}, R_c = R_{X12}$.

Proof. See Appendix C.

Now using Lemma 1, we show how to construct scalable qutrit circuits for block diagonal special unitaries. Let $U \in SU(3^n)$ be a block diagonal special unitary matrix with 3×3 special unitary diagonal blocks. In other words,

$$U = \begin{bmatrix} U_1(\Lambda_1) & & & \\ & U_2(\Lambda_2) & & \\ & & \ddots & \\ & & & U_{3^{n-1}}(\Lambda_{3^{n-1}}) \end{bmatrix}, \quad (33)$$

where $\Lambda_j := (\theta_1^{(j)}, \phi_1^{(j)}, \psi_1^{(j)}, \theta_2^{(j)}, \phi_2^{(j)}, \psi_2^{(j)}, \theta_3^{(j)}, \phi_3^{(j)}, \psi_3^{(j)})$ and each $U_j(\Lambda_j) \in SU(3)$. Then clearly from proof of

Theorem 1 in Appendix A and Eq. (A4), we have

$$U = U_1 U_2 U_3, \tag{34}$$

where U_1, U_2, U_3 are block-diagonal special unitary matrices with each block belonging to SU(3) such that

$$U_j = \begin{bmatrix} M_j(-\theta_j^{(1)}, -\phi_j^{(1)}, \psi_j^{(1)}) & & \\ & \ddots & \\ & & M_j(-\theta_j^{(3^{n-1})}, -\phi_j^{(3^{n-1})}, \psi_j^{(3^{n-1})}) \end{bmatrix} \tag{35}$$

for some $\theta_j^{(k)}, \phi_j^{(k)}, \psi_j^{(k)}$ $j \in \{1, 2, 3\}$ and $k \in \{1, 2 \ldots, 3^{n-1}\}$. In order to construct qutrit circuit of U, we will look at the circuits for each of its components on the right-hand side in Eq. (34), i.e., U_j in Eq. (35).

Theorem 3. The qutrit circuit for U_j, $j \in \{1, 2, 3\}$ in Eq. (34) and Eq. (35) is given by

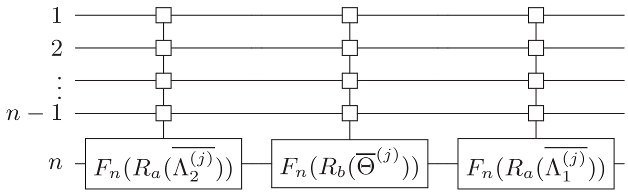

(36)

$$\text{where } \begin{cases} R_a = R_{Z02}, R_b = R_{Y02}, & \text{if } j = 1, \\ R_a = R_{Z01}, R_b = R_{Y01}, & \text{if } j = 2, \\ R_a = R_{Z12}, R_b = R_{Y12}, & \text{if } j = 3 \end{cases} \quad \text{such that}$$

$$\overline{\Theta^{(j)}} = \big(-\theta_j^{(1)}, \ldots, -\theta_j^{(3^{n-1})}\big),$$

$$\overline{\Lambda_1^{(j)}} = \left(\frac{-\phi_j^{(1)} + \psi_j^{(1)}}{2}, \ldots, \frac{-\phi_j^{(3^{n-1})} + \psi_j^{(3^{n-1})}}{2}\right),$$

$$\overline{\Lambda_2^{(j)}} = \left(\frac{-\phi_j^{(1)} - \psi_j^{(1)}}{2}, \ldots, \frac{-\phi_j^{(3^{n-1})} - \psi_j^{(3^{n-1})}}{2}\right),$$

and $\phi_2^{(k)} = 0 \forall k \in \{1, \ldots, 3^{n-1}\}$

Proof. Follows from Eqs. (A1), (A2), (A3) from the proof of Theorem 1 in Appendix A and from the construction of qutrit block-diagonal rotations. ■

From the discussions so far, we are now ready to provide a scalable circuit construction of multicontrolled qutrit-X gates using single-qutrit gates and controlled qutrit-X gates. Let us take the following multicontrolled n-qutrit-X gate used in construction of quantum qutrit circuits of three-state DTQWs of Cayley graphs discussed before.

Note that the gate

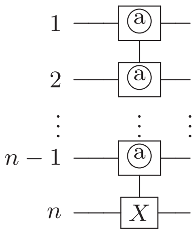

(37)

is equivalent to the following gates

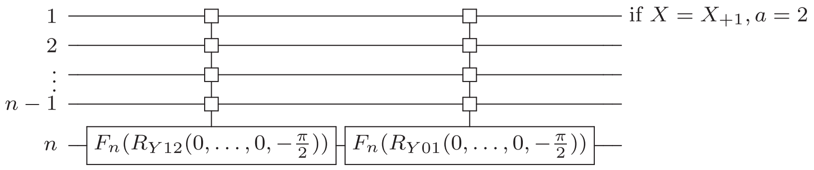

(38)

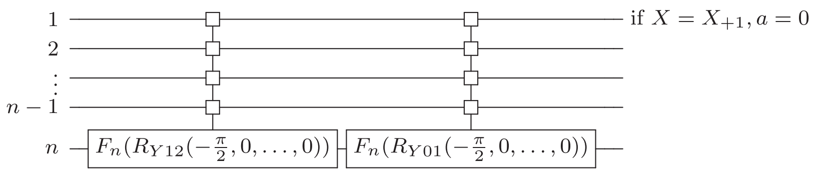

(39)

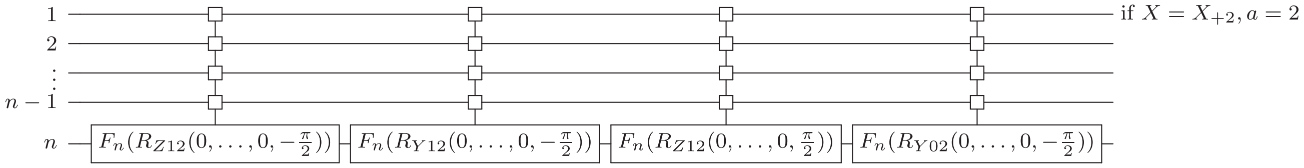

(40)

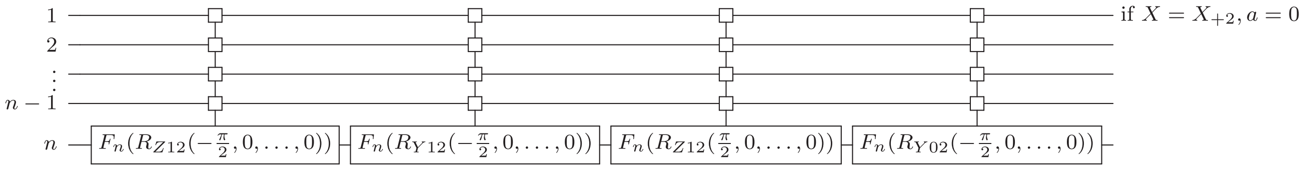

(41)

respectively

So far we have constructed ancilla free circuits of the n-qutrit block-diagonal special unitaries with special unitary blocks. However, the quantum circuit for DTQWs as derived above require the quantum gates given by

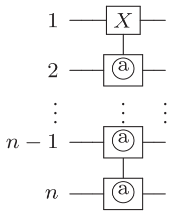

(42)

where $X \in \{X_{+1}, X_{+2}\}$, $a \in \{0, 2\}$. Hence, it is imperative that we express the qutrit gates in Eq. (42), in terms of multicontrolled n-qutrit-X gates. The main problem boils down to find unitary matrices P_1, P_2 such that

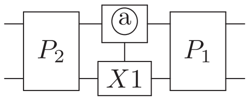

(43)

implements

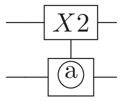

(44)

where $X1, X2$ are one-qutrit-X gates mentioned in Eq. (8) and $a \in \{0, 1, 2\}$.

To resolve this we first define the following circuit:

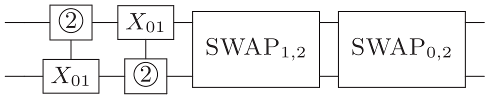

(45)

then have the following theorem.

Theorem 4. Let $P \in U(9)$ be a permutation matrix given by $P = P_{(3,8)}P_{(6,7)}$ where $P_{(i,j)}$ represents a two cycle permutation with ith and jth rows interchanged. Then setting $P_1 = P_2 = P$, the circuits in Eqs. (43) and (44) are equivalent for the following two cases. $\{\begin{smallmatrix} a = 2, X1 = X_{+1}, X2 = X_{+2} \text{ or,} \\ a = 2, X1 = X_{+2}, X2 = X_{+1}. \end{smallmatrix}$

Further the circuit of P is given by Eq. (45).

Proof. The proof is trivial follows by mapping the input and output states for the circuits. ■

It is to be noted that the n-qutrit circuit, given by

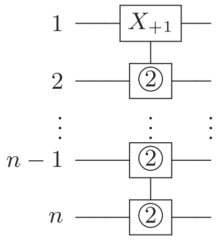

(46)

can be written as

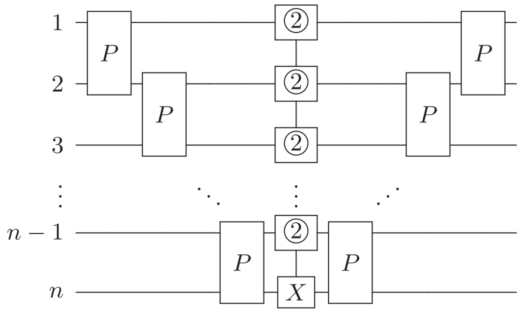

(47)

where $X = \{\begin{smallmatrix} X_{+2} \text{ if n is odd} \\ X_{+1} \text{ otherwise.} \end{smallmatrix}$

Finally, we recall that the circuit

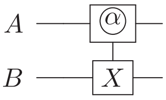

is equivalent to the circuit

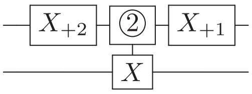

Thus, from our discussion so far, the qutrit gate

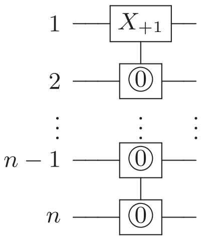

(48)

is equivalent to

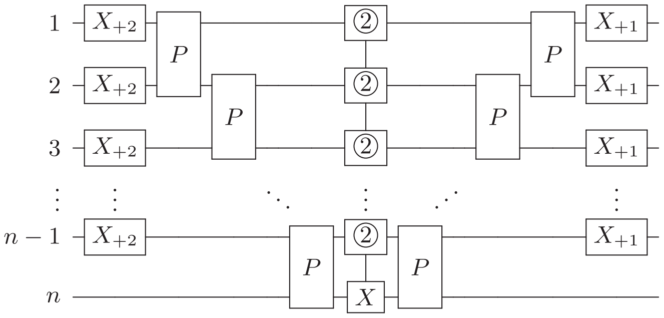

(49)

where $X = \begin{cases} X_{+2} & \text{if n is odd} \\ X_{+1} & \text{otherwise.} \end{cases}$

This concludes the construction of quantum circuit model of the DTQWs on Cayley graphs considered in this paper using single-qutrit rotation gates and controlled qutrit gates.

Remark 4. We observe that the qutrit circuit models developed above can also be derived for other DTQW models on other graphs when the walk can be studied by converting the time-space into Fourier space.

A. Circuit complexity of the models

In this section we discuss the circuit complexity of the quantum circuit models for the DTQWs developed above. This includes the number of elementary gates that are needed to implement the circuits for the cycle graphs, i.e., $\text{Cay}(\mathbb{Z}_N, \{1, -1\})$ and the Cayley graphs $\text{Cay}(D_N, \{\mu, \xi\})$ where $3^{n-1} \leqslant N \leqslant 3^n$. Note that a time step of a DTQW is same as one layer in the circuit model for the implementation of t-step quantum walks, $t \geqslant 1$.

Moreover, the primary gates that are used in the design of the circuits are multicontrolled X gates (generalized Toffoli gates), which correspond to the construction of the circuits for block-diagonal unitary matrices, and the gates INCREMENT, DECREMENT, DESTOP, INSTOP, and RC.

First we have the following result for multicontrolled X gates.

Theorem 5. The multicontrolled X gates described in Eqs. (27) and (28), where $X \in \{X_{+1}, X_{+2}\}$ need $O(4 \cdot 3^{n-1})$ two-qutrit controlled-X gates and $O(2 \cdot 3^{n-1})$ one-qutrit rotation gates.

Proof. Follows from using simple induction on the number of gates and the proof directly follows from Eq. (37) and its equivalent circuits starting from Eq. (38), Lemma 1, construction of qutrit SWAP gates and Theorem 4. ■

From the construction of multicontrolled qutrit gates, it is obvious that that more number of two-qutrit controlled-X gates or M-S gates are always used if we want more number of standard basis elements to remain invariant under multicontrolled qutrit gate transformation. Hence, it is obvious that a circuit like

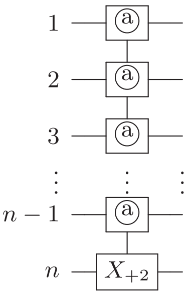

(49)

comprises of more number of two-qutrit controlled-X gates or M-S gates than that a circuit like

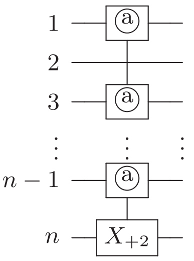

(50)

where $a \in \{0, 1, 2\}$.

We also note that, the circuit

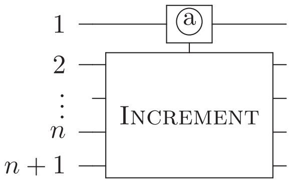

(51)

is equivalent to

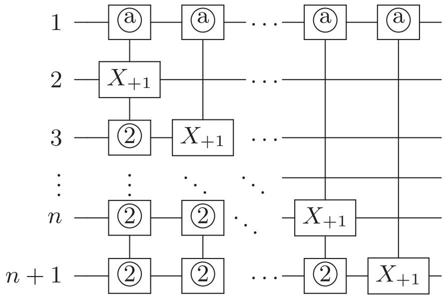

(52)

Besides, we know that

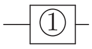

is equivalent to

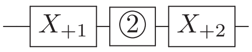

Similar argument is also valid when we replace INCREMENT by DECREMENT as well. Further, we see that constructing a general one-qutrit gate (special unitary matrix) requires nine one-qutrit rotation gates. Thus we have the following theorem.

Theorem 6. A single layer (one time-step) of DTQW on $\mathrm{Cay}(D_N, \{\mu, \xi\})$ where $N = 3^n$ requires $O(8n3^{n+1} + 2)$ two-qutrit controlled-X gates and $O(4 \times 3^{n+1})$ one-qutrit rotation gates.

Proof. Follows from the argument above and Theorem 5.■

Remark 5.

(1) Since constructing gates like DESTOP and INSTOP require a sequence of multicontrolled qutrit-X gates, it is clear from Theorem 5 that the number of two-qutrit controlled-X gates required for constructing such gates is $O[4p(n)3^{n-1}]$ for some polynomial p. Hence, we get the following result trivially that a single layer (time step) of DTQW on $\mathrm{Cay}(D_N, \{\mu, \xi\})$, $3^{n-1} \leqslant N < 3^n$ requires $O\{8[n + p(n)]3^{n+1}\}$ two-qutrit controlled-X gates and $O\{4[n + q(n)]3^{n+1}\}$ one-qutrit rotation gates, where p, q are some polynomials in n.

(2) Similar results can be obtained for three-state lively DTQWs on cycles, i.e., $\mathrm{Cay}(\mathbb{Z}_N, \{1, -1\})$, however, it is to be observed that for nonzero liveliness parameter a, by the same argument used so far, the gate $\mathrm{RC}(a)$ requires $O(4na3^{n-1})$ two-qutrit controlled-X gates. Further, unlike DTQW on Cayley graphs of dihedral groups which is a $(n + 2)$-qutrit circuit, this circuit is a unitary matrix of order $3^{n+1} \times 3^{n+1}$. From this, we find that a single layer (one time step) of three-state lively DTQW on $\mathrm{Cay}(\mathbb{Z}_N, \{1, -1\})$, $N = 3^n, a \leqslant \lfloor \frac{N}{2} \rfloor$, $O[(8n + 4na)3^n]$ two-qutrit controlled-X gates and $O(4na3^n)$ one-qutrit rotation gates.

(3) When $N \neq 3^n$ however, a single layer (time step) of three-state lively DTQW on $\mathrm{Cay}(\mathbb{Z}_N, \{1, -1\})$, $3^{n-1} \leqslant N < 3^n, a \leqslant \lfloor \frac{N}{2} \rfloor$ requires $O\{4[na + f(n)]3^n|\}$ two-qutrit controlled-X gates and $O\{4[na + g(n)]3^n\}$ one-qutrit rotation gates, where f, g are some polynomials in n.

All of these results are trivial and follow immediately using Theorem 5 and Theorem 6.

Finally, we prove one result for quantum circuit complexity of constructing block-diagonal special unitary matrices with special unitary blocks. Such matrices are seldom used in sparse matrix decomposition and hence, are important.

Theorem 7. Let $U \in \mathrm{SU}(3^n)$ be a block-diagonal special unitary matrix with 3×3 special unitary diagonal blocks. Then the quantum circuit for U requires $O(2 \times 3^{n+1})$ two-qutrit controlled-X gates and $O(3^{n+1})$ one-qutrit rotation gates.

Proof. The proof follows from Lemma 1 and Eqs. (34) and (35). ■

In the following section we numerically simulate these quantum circuits by inducing generic noise models in order to replicate its output which would be obtained in a noisy quantum computer.

V. NOISY SIMULATION OF THE CIRCUIT MODEL

In this section, we report numerical simulation results based on the circuit models as obtained above. The simulations are performed incorporating noise models in order to mimic a noisy quantum computer such as noisy intermediate scale quantum (NISC) computers for implementation of the qutrit model of the DTQWs on $\mathrm{Cay}(D_N, \{\mu, \xi\})$ and $\mathrm{Cay}(\mathbb{Z}_N, \{1, -1\})$. This noise includes gate error and idle error, which are standard practice for numerical simulation of quantum circuits [22]. Further, in order to investigate and verify the simulations results and the analytical results obtained in the literature, we consider a family of one-parameter coins for the DTQWs, known as generalized Grover coins. See Ref. [41] for a more on generalized Grover coins.

The generalized Grover coin matrices of order 3 are orthogonal matrices that can be expressed as linear sum of permutation matrices. These matrices are divided into four classes as described below.

$$\mathcal{X}_\theta = \left\{ \begin{bmatrix} \frac{2\cos\theta+1}{3} & \frac{1-\cos\theta}{3} + \frac{\sin\theta}{\sqrt{3}} & \frac{1-\cos\theta}{3} - \frac{\sin\theta}{\sqrt{3}} \\ \frac{1-\cos\theta}{3} - \frac{\sin\theta}{\sqrt{3}} & \frac{2\cos\theta+1}{3} & \frac{1-\cos\theta}{3} + \frac{\sin\theta}{\sqrt{3}} \\ \frac{1-\cos\theta}{3} + \frac{\sin\theta}{\sqrt{3}} & \frac{1-\cos\theta}{3} - \frac{\sin\theta}{\sqrt{3}} & \frac{2\cos\theta+1}{3} \end{bmatrix} : -\pi < \theta \leqslant \pi \right\}, \tag{53}$$

$$\mathcal{Y}_\theta = \left\{ \begin{bmatrix} \frac{2\cos\theta-1}{3} & \frac{-1-\cos\theta}{3} + \frac{\sin\theta}{\sqrt{3}} & \frac{-1-\cos\theta}{3} - \frac{\sin\theta}{\sqrt{3}} \\ \frac{-1-\cos\theta}{3} - \frac{\sin\theta}{\sqrt{3}} & \frac{2\cos\theta-1}{3} & \frac{-1-\cos\theta}{3} + \frac{\sin\theta}{\sqrt{3}} \\ \frac{-1-\cos\theta}{3} + \frac{\sin\theta}{\sqrt{3}} & \frac{-1-\cos\theta}{3} - \frac{\sin\theta}{\sqrt{3}} & \frac{2\cos\theta-1}{3} \end{bmatrix} : -\pi < \theta \leqslant \pi \right\}, \tag{54}$$

$$\mathcal{Z}_\theta = \left\{ \begin{bmatrix} \frac{2\cos\theta+1}{3} & \frac{1-\cos\theta}{3} + \frac{\sin\theta}{\sqrt{3}} & \frac{1-\cos\theta}{3} - \frac{\sin\theta}{\sqrt{3}} \\ \frac{1-\cos\theta}{3} + \frac{\sin\theta}{\sqrt{3}} & \frac{1-\cos\theta}{3} - \frac{\sin\theta}{\sqrt{3}} & \frac{2\cos\theta+1}{3} \\ \frac{1-\cos\theta}{3} - \frac{\sin\theta}{\sqrt{3}} & \frac{2\cos\theta+1}{3} & \frac{1-\cos\theta}{3} + \frac{\sin\theta}{\sqrt{3}} \end{bmatrix} : -\pi < \theta \leqslant \pi \right\}, \tag{55}$$

$$\mathcal{W}_\theta = \left\{ \begin{bmatrix} \frac{2\cos\theta-1}{3} & \frac{-1-\cos\theta}{3} + \frac{\sin\theta}{\sqrt{3}} & \frac{-1-\cos\theta}{3} - \frac{\sin\theta}{\sqrt{3}} \\ \frac{-1-\cos\theta}{3} + \frac{\sin\theta}{\sqrt{3}} & \frac{-1-\cos\theta}{3} - \frac{\sin\theta}{\sqrt{3}} & \frac{2\cos\theta-1}{3} \\ \frac{-1-\cos\theta}{3} - \frac{\sin\theta}{\sqrt{3}} & \frac{2\cos\theta-1}{3} & \frac{-1-\cos\theta}{3} + \frac{\sin\theta}{\sqrt{3}} \end{bmatrix} : -\pi < \theta \leqslant \pi \right\}. \tag{56}$$

The Grover matrix of order 3 given by

$$\mathsf{G} = \begin{bmatrix} \frac{-1}{3} & \frac{2}{3} & \frac{2}{3} \\ \frac{2}{3} & \frac{-1}{3} & \frac{2}{3} \\ \frac{2}{3} & \frac{2}{3} & \frac{-1}{3} \end{bmatrix} \in \mathcal{X}_\theta$$

by setting $\theta = \pi$.

We also corroborate our results on localization pertaining to DTQWs on Cayley graphs obtained in Ref. [12]. All simulations have been done in MATLAB2019A on a system with 16 GB RAM, Intel(R) Core(TM) i5 - 035G1 CPU @1.00 GHz 1.19 GHz processor.

A. Noise models

The noise in the gate and idle errors are incorporated through the use of Kraus operators. Kraus operators are a set of positive semidefinite matrices $\{E_j | j \subset \mathbb{N}\}$, such that the time evolution of a quantum system with initial state density matrix $\sigma = |\psi(0)\rangle\langle\psi(0)|$ is expressed as a function $E(\sigma) = \sum_j E_j \sigma E_j^\star$, where $\star$ denotes the transpose. We follow the operators discussed in Refs. [22,50].

1. Gate noise

For qutrits, taking $X_{+1} = \begin{bmatrix} 0 & 0 & 1 \\ 1 & 0 & 0 \\ 0 & 1 & 0 \end{bmatrix}$ and $Z_3 = \begin{bmatrix} 1 & 0 & 0 \\ 0 & \exp(i2\pi/3) & 0 \\ 0 & 0 & \exp(i4\pi/3) \end{bmatrix}$, the depolarizer gate error for single-qutrit gate is defined as

$$E_{G1}(\sigma) = \Big(I - \sum_{j,k\in\{0,1,2\}} p_{jk}\sigma\Big) + \sum_{j,k\in\{0,1,2\}} p_{jk}\big(X_{+1}^j Z_3^k\big)\sigma\big(X_{+1}^j Z_3^k\big)^\star. \quad (57)$$

We assume the probabilities of all the error terms to be equal to p_1. Then the Eq. (58) can be rewritten as

$$E_{G1}(\sigma) = (I - 9p_1\sigma) + \sum_{j,k\in\{0,1,2\}} p_1\big(X_{+1}^j Z_3^k\big)\sigma\big(X_{+1}^j Z_3^k\big)^*. \quad (58)$$

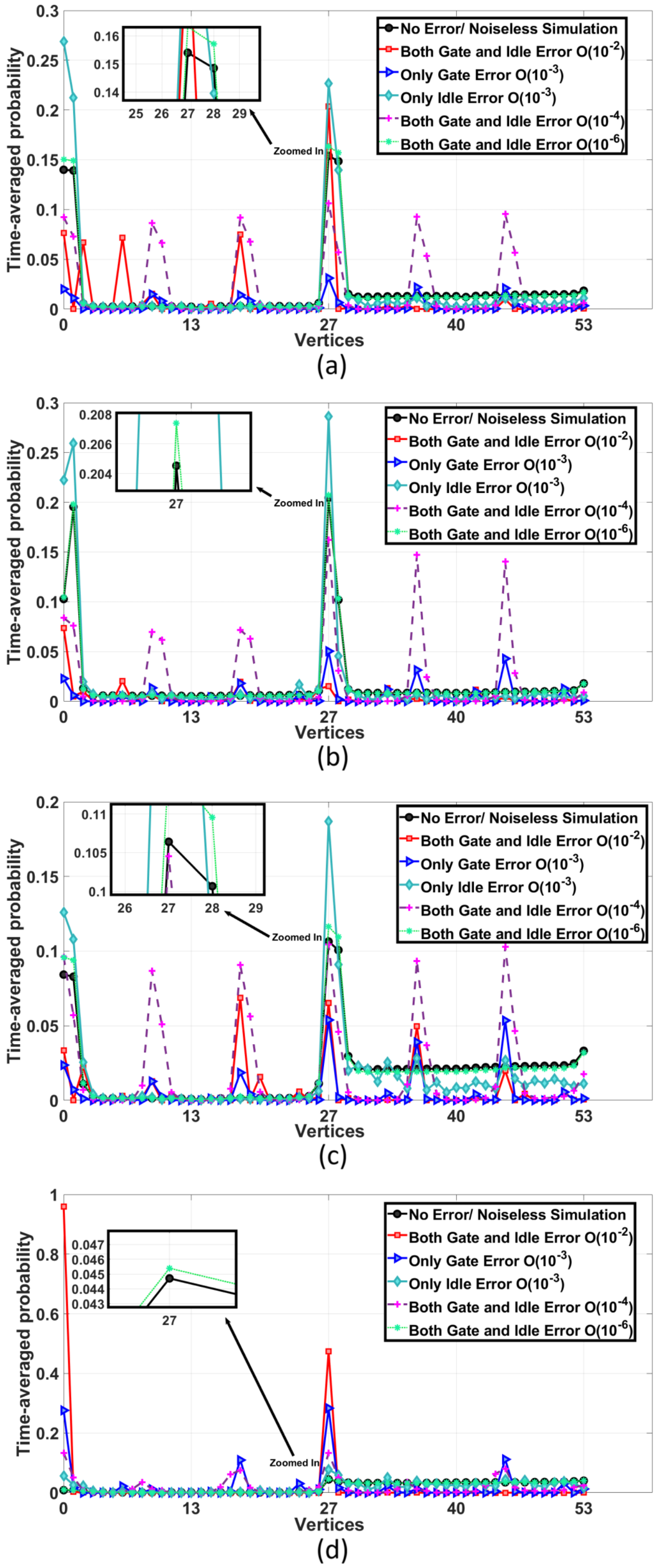

FIG. 2. Time-averaged probability for Cay($D_{27}, \{\mu, \xi\}$) taking coins from the classes , $\mathcal{X}_\theta, \mathcal{Y}_\theta, \mathcal{Z}_\theta, \mathcal{W}_\theta$ with initial position (1,0) and initial coin state $|0\rangle_3$. The time step is taken up to 300. The generic depolarizer gate noise and amplitude damping idle noise is incorporated in the circuit. In (a), $C \in \mathcal{X}_\theta$, $\theta = \pi$, i.e., the coin is the Grover matrix. In (b), $C \in \mathcal{Y}_\theta$, $\theta = \pi/2$. In (c), $C \in \mathcal{Z}_\theta$, $\theta = \pi/3$. In (d), $C \in \mathcal{W}_\theta$, $\theta = -\pi/4$. In the figures, the solid black line with ○ markers denotes the noiseless or ideal time-averaged probability. The solid red line with □ markers depicts the time-averaged probability when both gate and idle errors are of order $O(10^{-2})$. The solid blue line with ▷ markers denotes the time-averaged probability when only gate error of $O(10^{-3})$ strength is present in the circuit and the turquoise solid line with ◇ markers is the plot of the time-averaged probability when only idle error of $O(10^{-3})$ strength is present in the circuit. The magenta dashed line with + markers and the dotted green line with ∗ markers are the plots of time-averaged probability when both gate and idle errors are of order $O(10^{-4})$ and $O(10^{-6})$, respectively. The insets introduced in the figures are a zoomed-in version of the plots depicting the extremely minute deviation between the time-averaged probability at the localized vertex of a noiseless circuit and a circuit with gate and idle error of order $O(10^{-6})$ or less.

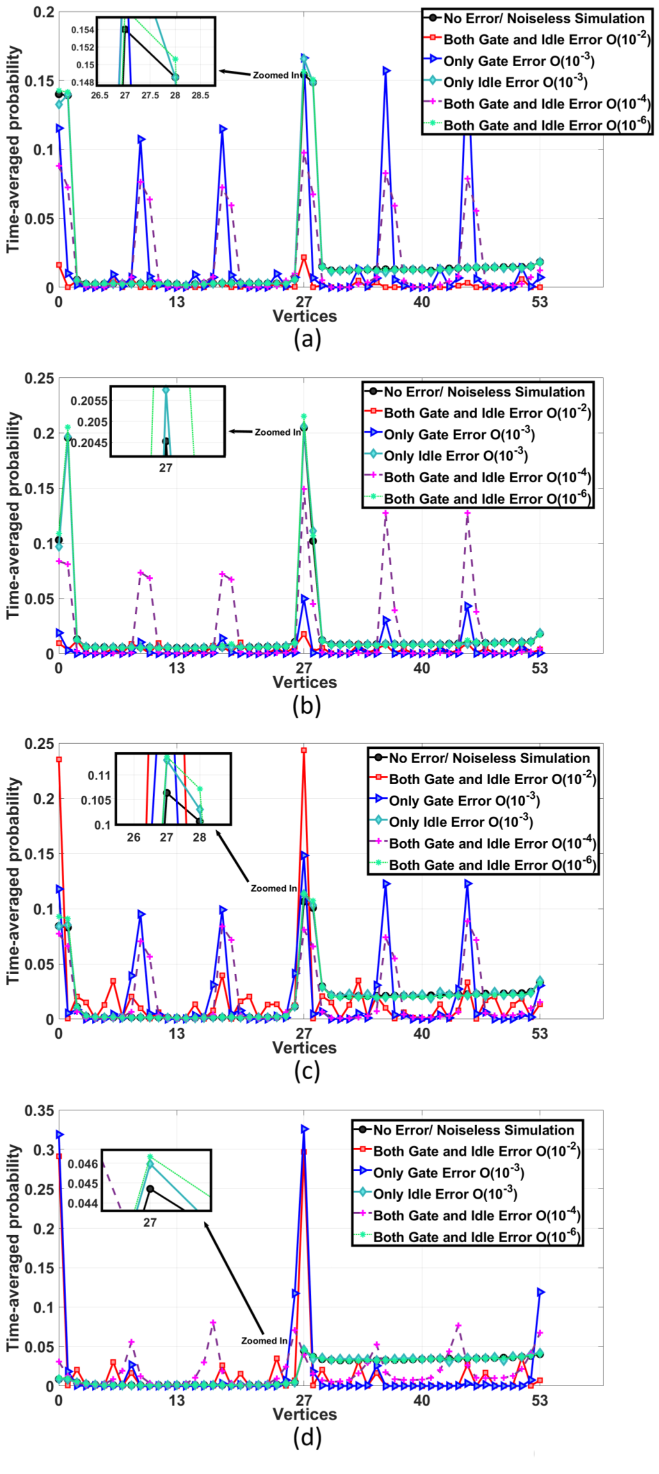

FIG. 3. Time averaged probability for Cay($D_{27}, \{\mu, \xi\}$) taking coins from the classes , $\mathcal{X}_\theta, \mathcal{Y}_\theta, \mathcal{Z}_\theta, \mathcal{W}_\theta$ with initial position (1,0) and initial coin state $|0\rangle_3$. The time step is taken up to 300. The generic depolarizer gate noise and phase damping idle noise is incorporated in the circuit. The error parameters are chosen from uniform distribution. In (a), $C \in \mathcal{X}_\theta, \theta = \pi$, i.e., the coin is the Grover matrix. In (b), $C \in \mathcal{Y}_\theta, \theta = \pi/2$. In (c), $C \in \mathcal{Z}_\theta, \theta = \pi/3$. In (d), $C \in \mathcal{W}_\theta, \theta = -\pi/4$. The solid black line with $\circ$ markers denotes the noiseless or ideal time-averaged probability. The solid red line with $\square$ markers depicts the time-averaged probability when both gate and idle errors are of order $O(10^{-2})$. The solid blue line with $\triangleright$ markers denotes the time-averaged probability when only gate error of $O(10^{-3})$ strength is present in the circuit and the turquoise solid line with $\diamond$ markers is the plot of the time-averaged probability when only idle error of $O(10^{-3})$ strength is present in the circuit. The magenta dashed line with $+$ markers and the dotted green line with $*$ markers are the plots of time-averaged probability when both gate and idle errors are of order $O(10^{-4})$ and $O(10^{-6})$ respectively. The insets introduced in the figures are a zoomed-in version of the plots depicting the extremely small deviation between the time-averaged probability of a noiseless circuit and a circuit with gate and idle error of order $O(10^{-6})$ or less.

For n-qutrit gates, the gate error is defined as

$$E_{Gn}(\sigma) = \left(\sum_{a_1,a_2,\dots,a_n,b_1,b_2,\dots b_n\in\{0,1,2\}} p_1 E_{a_1b_1a_2b_2\dots a_nb_n}\sigma E^{\star}_{a_1b_1a_2b_2\dots a_nb_n}\right) + (I - 3^{2n}p_1\sigma), \tag{59}$$

where $E_{a_1b_1a_2b_2\dots a_nb_n} = \otimes_{j=1}^{n} X_{+1}^{a_j} Z_3^{b_j}$.

2. *Idle error*

Idle errors occur from decoherence of a quantum system that arises with interaction with the environment. Idle errors such as amplitude and phase damping errors are incorporated for excited qutrits. Some variants of idle errors are presented here.

(1) Amplitude damping: In a mathematical sense, amplitude damping idle errors are represented using the expression

$$K_A(\sigma) = \sum_{j\in\{0,1,2\}} K_j\sigma K_j^*. \tag{60}$$

set of Kraus operators $\{K_j\}$ such that $\sum_j K_jK_j^* = I$ and

$$K_0(t) = \begin{bmatrix} 1 & 0 & 0 \\ 0 & \sqrt{\exp(-r_1t)} & 0 \\ 0 & 0 & \sqrt{\exp(-r_2t)} \end{bmatrix}, \tag{61}$$

$$K_1(t) = \begin{bmatrix} 0 & \sqrt{1-\exp(-r_1t)} & 0 \\ 0 & 0 & 0 \\ 0 & 0 & 0 \end{bmatrix}, \tag{62}$$

$$K_2(t) = \begin{bmatrix} 0 & 0 & \sqrt{1-\exp(-r_2t)} \\ 0 & 0 & 0 \\ 0 & 0 & 0 \end{bmatrix}, \tag{63}$$

where $r_1, r_2, > 0$ are error parameters.

(2) Phase damping: Similar to amplitude damping, the phase damping idle errors are represented using the expression

$$E_A(\sigma) = \sum_{j\in\{0,1\}} K_j\sigma K_j^* \tag{64}$$

set of Kraus operators $\{K_j\}$ such that $\sum_j K_jK_j^* = I$ and $K_0(t) = \sqrt{\exp(-r_1t)}I, K_1(t) = \sqrt{1-\exp(-r_1t)}Z_3$, where $r_1 > 0$.

Now, we will incorporate these errors in to our circuit and numerically simulate it in order to see the effect of various errors on localization of the walk.

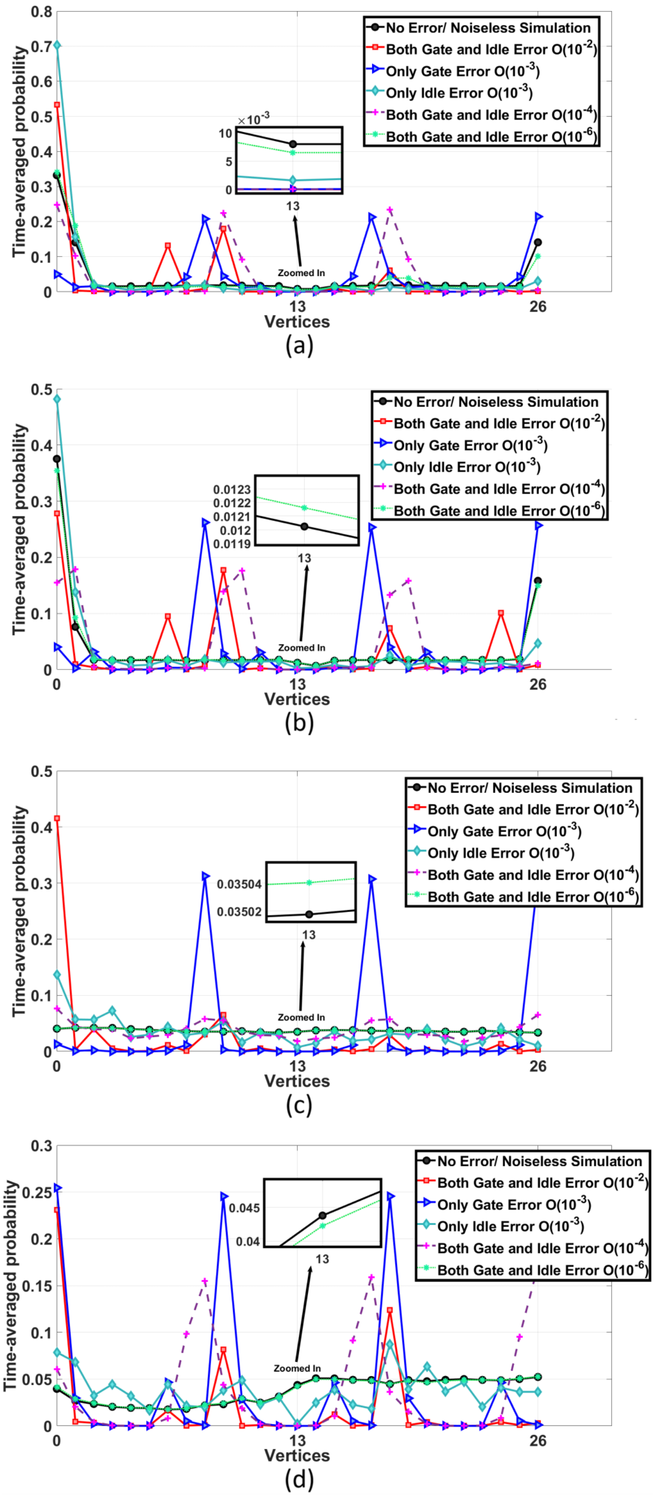

(a)

(b)

(c)

(d)

FIG. 4. Time-averaged probability for Cay($\mathbb{Z}_{27}$, {1, −1}) taking coins from the classes , $\mathcal{X}_\theta, \mathcal{Y}_\theta, \mathcal{Z}_\theta, \mathcal{W}_\theta$ with initial position 0 and initial coin state $\frac{1}{\sqrt{3}}(|0\rangle_3 + |1\rangle_3 + |2\rangle_3)$. The time step is taken up to 300. The generic depolarizer gate noise and amplitude damping idle noise is incorporated in the circuit. The error parameters are chosen from uniform distribution. In (a), $C \in \mathcal{X}_\theta, \theta = \pi$, i.e., the coin is the Grover matrix. In (b), $C \in \mathcal{Y}_\theta, \theta = \pi/2$. In (c), $C \in \mathcal{Z}_\theta, \theta = \pi/3$. In (d), $C \in \mathcal{W}_\theta, \theta = -\pi/4$. The solid black line with ○ markers denotes the noiseless or ideal time-averaged probability. The solid red line with □ markers depicts the time-averaged probability when both gate and idle errors are of order $O(10^{-2})$. The solid blue line with ▷ markers denotes the time-averaged probability when only gate error of $O(10^{-3})$ strength is present in the circuit and the turquoise solid line with ◇ markers is the plot of the time-averaged probability when only idle error of $O(10^{-3})$ strength is present in the circuit. The magenta dashed line with + markers and the dotted green line with $*$ markers are the plots of time-averaged probability when both gate and idle errors are of order $O(10^{-4})$ and $O(10^{-6})$, respectively. The insets in the figures are a zoomed-in version of the plots depicting the small difference between the time-averaged probability of a noiseless circuit and a circuit with gate and idle error of order $O(10^{-6})$ or less.

B. Numerical simulation of three-state DTQW on Cay(D_{27}, {μ, ξ})

We corroborate our results from Ref. [12] on time-averaged probability of three-state quantum walks and periodicity of Cay(D_N, {μ, ξ}) where $N = 27$. We recall that the unitary matrix corresponding to increment and decrement gates are

$$\text{INCREMENT} = \left[\begin{array}{c|c} 0_{1\times 26} & 1 \\ \hline I_{26} & 0_{26\times 1} \end{array}\right], \tag{65}$$

$$\text{DECREMENT} = \left[\begin{array}{c|c} 0_{26\times 1} & I_{26} \\ \hline 1 & 0_{1\times 26} \end{array}\right]. \tag{66}$$

The unitary matrix for the circuit

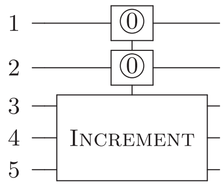

(67)

is given by

$$U_{In} = \left[\begin{array}{c|c} \text{INCREMENT} & 0_{27\times 216} \\ \hline 0_{216\times 27} & I_{216} \end{array}\right]. \tag{68}$$

Similarly, the unitary matrix for the circuit

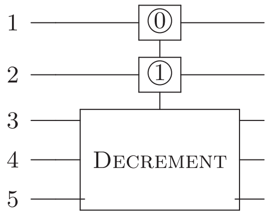

(69)

is given by

$$U_{De} = \left[\begin{array}{c|c|c} I_{27} & O_{27\times 27} & O_{27\times 189} \\ \hline O_{27\times 27} & \text{DECREMENT} & O_{27\times 189} \\ \hline O_{189\times 27} & O_{27\times 27} & I_{189} \end{array}\right]. \tag{70}$$

In Fig. 2, we plot the time-averaged probability of finding a particle at all vertices of Cay(D_{27}, {μ, ξ}) for the initial coin state $|0\rangle_3$ and starting vertex (1,0). In the first figure the coin C is taken from the class $\mathcal{X}_\theta$ where $\theta = \pi$, i.e., the coin is the Grover coin G. In the subsequent figures, the coin C is taken from the class $\mathcal{Y}_\theta$ where $\theta = \pi/2$, $C \in \mathcal{Z}_\theta, \theta = \pi/3$, and $C \in \mathcal{W}_\theta, \theta = -\pi/4$, respectively. We incorporate the gate error and amplitude damping idle error in order to replicate the output, which would be typically found in a near-term

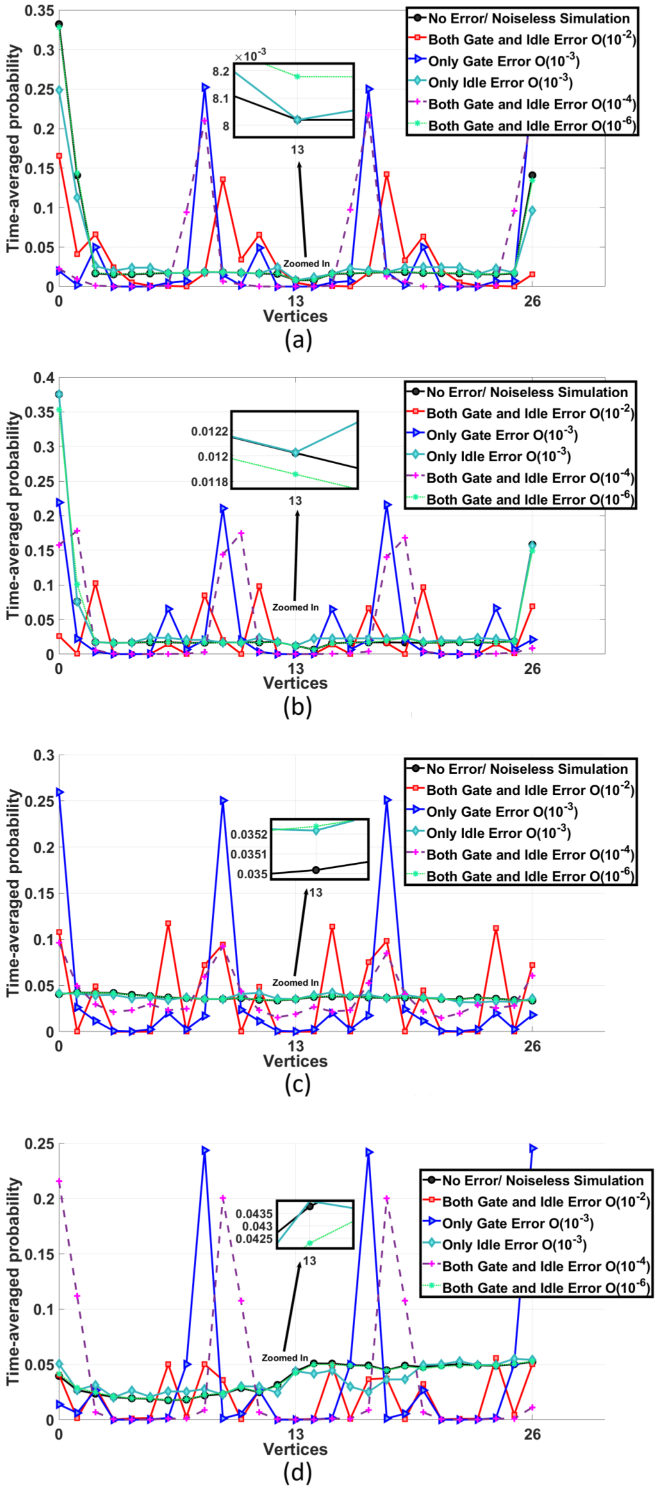

FIG. 5. Time-averaged probability for Cay($\mathbb{Z}_{27}$, $\{1, -1\}$) taking coins from the classes , $\mathcal{X}_\theta, \mathcal{Y}_\theta, \mathcal{Z}_\theta, \mathcal{W}_\theta$ with initial position 0 and initial coin state $\frac{1}{\sqrt{3}}(|0\rangle_3 + |1\rangle_3 + |2\rangle_3)$. The time step is taken up to 300. The generic depolarizer gate noise and phase damping idle noise is incorporated in the circuit. The error parameters are chosen from the uniform distribution. In (a), $C \in \mathcal{X}_\theta, \theta = \pi$, i.e., the coin is the Grover matrix. In (b), $C \in \mathcal{Y}_\theta, \theta = \pi/2$. In (c), $C \in \mathcal{Z}_\theta, \theta = \pi/3$. In (d), $C \in \mathcal{W}_\theta, \theta = -\pi/4$.The solid black line with $\circ$ markers denotes the noiseless or ideal time-averaged probability. The solid red line with $\square$ markers depicts the time-averaged probability when both gate and idle errors are of order $O(10^{-2})$. The solid blue line with $\triangleright$ markers denotes the time-averaged probability when only gate error of $O(10^{-3})$ strength is present in the circuit and the turquoise solid line with $\diamond$ markers is the plot of the time-averaged probability when only idle error of $O(10^{-3})$ strength is present in the circuit. The magenta dashed line with $+$ markers and the dotted green line with $*$ markers are the plots of time-averaged probability when both gate and idle errors are of order $O(10^{-4})$ and $O(10^{-6})$, respectively. The insets introduced in the figures are a zoomed-in version of the plots showing the little difference between the time-averaged probability of a noiseless circuit and a circuit with gate and idle error of order $O(10^{-6})$ or less.

quantum computer. We incorporate varying degrees of error and see how much the result deviates from the result obtained via noiseless simulation. First we run a noiseless simulation whose time-averaged probability is depicted by the solid black line with circular markers ($\circ$) in the figure, then we incorporate high values [$O(10^{-2})$] of gate error and idle error with the error parameters chosen at random from uniform distribution presented through the solid red line with square markers ($\square$). We also simulate the circuit by incorporating only gate error and only channel error of order $O(10^{-3})$, depicted by solid blue line with triangular markers, i.e., $\triangleright$ and solid Turquoise line with diamond markers, i.e., $\diamond$, respectively, to see the effect of individual errors on the simulation. Finally we simulate the circuit with very small values [$O(10^{-4})$ and $O(10^{-6})$] of gate and idle errors. The time-averaged probability corresponding to these error values are shown in the figure as dashed magenta line with plus markers ($+$) and dotted green line with asterisk markers ($*$). We notice that for high value of errors, the maximum probability of finding the walker on the graph is not necessarily found at the starting vertex or its reflection vertex as observed in noiseless simulation. It is also to be noted that the error parameters r_1, r_2, p_1 are chosen randomly via uniform distribution between 0 and $10^{-\epsilon}$ to generate an error of order $O(10^{-\epsilon-1})$ for some $\epsilon \in \mathbb{N}$. Similarly, in Fig. 3 we plot the time-averaged probability at various positions of the walk on Cay(D_{27}, $\{\mu, \xi\}$) with coin state $|0\rangle_3$ and starting vertex (1,0) and coin is taken from the classes $\mathcal{X}_\theta, \mathcal{Y}_\theta, \mathcal{Z}_\theta, \mathcal{W}_\theta$ for several values of θ as described in Fig. 2. The only difference is that we incorporate phase damping instead of the amplitude damping as the idle error and the error parameters are chosen from uniform distribution.

C. Numerical simulation of three-state lazy DTQW on Cay($\mathbb{Z}_{27}$, $\{1, -1\}$)

We perform numerical simulations pertaining to three-state lazy DTQWs on cycle graphs with 27 vertices. In Fig. 4 we plot the time-averaged probability of finding the quantum walker at vertices of Cay($\mathbb{Z}_{27}$, $\{1, -1\}$) for the initial coin state $\frac{1}{\sqrt{3}}(|0\rangle_3 + |1\rangle_3 + |2\rangle_3)$ and starting vertex 0. In the first figure the coin C is taken from the class $\mathcal{X}_\theta$ where $\theta = \pi$ (Grover coin G), $\mathcal{Y}_\theta$ where $\theta = \pi/2$, $C \in \mathcal{Z}_\theta, \theta = \pi/3$, and $C \in \mathcal{W}_\theta, \theta = -\pi/4$, respectively. Also, in Fig. 5, we plot same the time-averaged probability of finding a particle at all vertices of Cay($\mathbb{Z}_{27}$, $\{1, -1\}$) for the initial coin state $\frac{1}{\sqrt{3}}(|0\rangle_3 + |1\rangle_3 + |2\rangle_3)$ and starting vertex 0 and coin similar to Fig. 4. The idle error is taken to be phase damping instead of amplitude damping. We incorporate several gate and idle errors into our circuits similar to Fig. 2 and Fig. 3 with a similar phenomenon of the walker not localizing at the starting vertex being observed for high error values.

Remark 6. We also have performed numerical simulation based on the noise models for the cycle graph and Cayley graph corresponding to dihedral group with different number of nodes and different initial coin states. Those results validate the theoretical results obtained in Ref. [12].

Now in order to gain further insights from the above simulation results for the time-averaged probability distributions, we compare it for the noise models and noiseless simulation results. We consider the Kullback-Leibler divergence (KL divergence) and the total variation distance (TVD) for finding the distance between the probability distributions (in the unit bits). First we recall these measures as follows.

Let P, Q be two probability distributions for a discrete random variable X. Let $\mathcal{X}$ denote the range set of X. Then:

(1) KL divergence [51,52]:

$$D_{\rm KL}(P\|Q) = \sum_{x\in\mathcal{X}} P(x)\log_2\left(\frac{P(x)}{Q(x)}\right)$$

$$= -\sum_{x\in\mathcal{X}} P(x)\log_2\left(\frac{Q(x)}{P(x)}\right).$$

(2) Total variation distance [53]:

$$TVD(P\|Q) = \frac{1}{2}\sum_{x\in\mathcal{X}} |P(x) - Q(x)|.$$

We will denote the time-averaged probability distribution of the walker obtained via noiseless circuit as IDEAL, and NOISY for the time-averaged probability distribution obtained in a noisy quantum circuit.

In Fig. 6, we plot the KL divergence $D_{\rm KL}(\text{IDEAL}\|\text{NOISY})$ (left blue bar) and the total variation distance $TVD(\text{IDEAL}\|\text{NOISY})$ (right orange bar) between the noiseless and noisy time-average probability distributions for finding the walker over the vertices of Cay($D_{27}, \{\mu, \xi\}$) for the initial coin state $|0\rangle_3$ and starting vertex (1,0) as shown in Fig. 2 and Fig. 3. In the first figure the coin C is taken from the class $\mathcal{X}_\theta$ where $\theta = \pi$ i.e. the coin is the Grover coin G. In the subsequent figures, the coin C is taken from the class $\mathcal{Y}_\theta$ where $\theta = \pi/2$, $C \in \mathcal{Z}_\theta, \theta = \pi/3$, and $C \in \mathcal{W}_\theta, \theta = -\pi/4$, respectively. Further, amplitude damping idle error and the generic depolarizer gate noise are chosen as noise models. It is observed from the figure that the gate error plays a significant role in deviating from noiseless distribution. It is also interesting to notice that the idle error sometimes mitigates the effects of gate errors as we see that for several figures the second bars and columns are longer than the first despite the second columns containing no idle errors. The

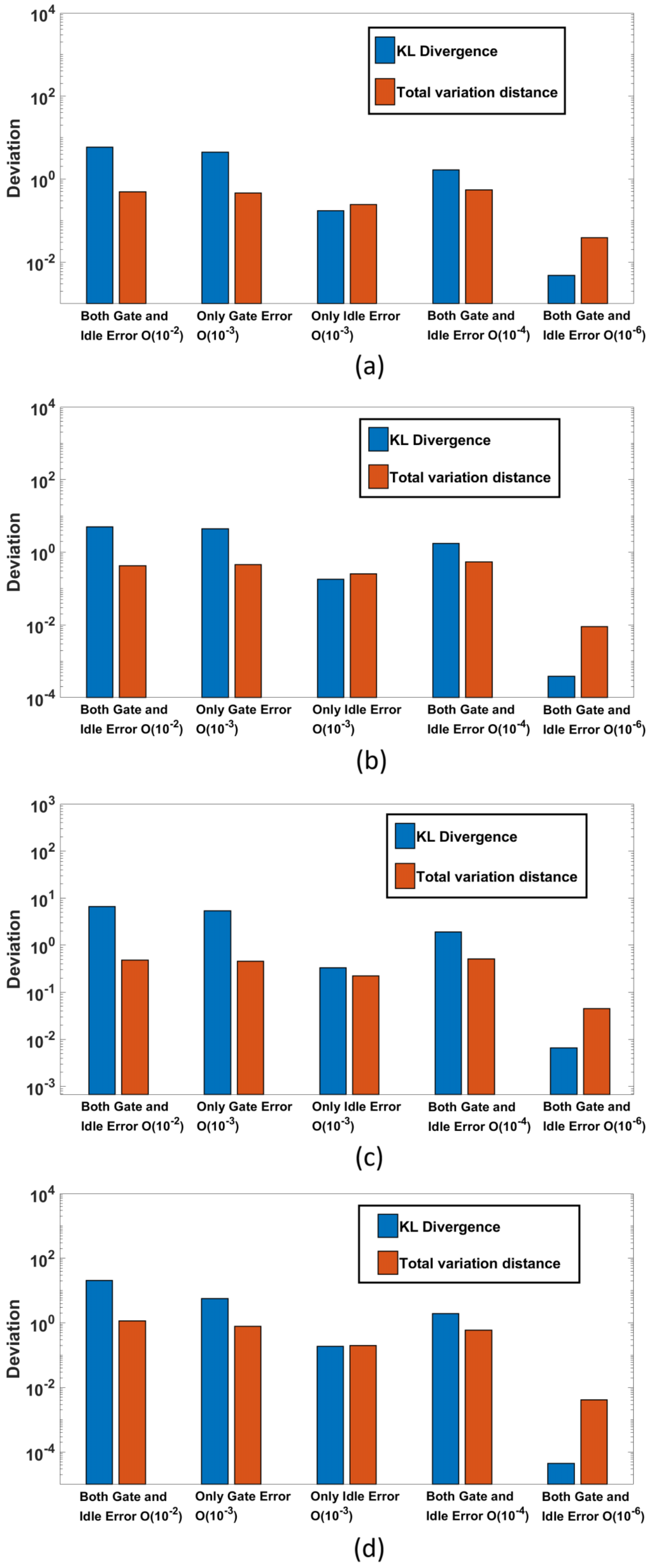

FIG. 6. Comparison $D_{\rm KL}(\text{IDEAL}\|\text{NOISY})$ (left blue bar) and $TVD(\text{IDEAL}\|\text{OISY})$ (right orange bar) between the time-averaged probability distributions obtained through noiseless and noisy circuits for DTQWs in Cay($D_{27}, \{\mu, \xi\}$) taking coins (denoted by C) from the classes , $\mathcal{X}_\theta, \mathcal{Y}_\theta, \mathcal{Z}_\theta, \mathcal{W}_\theta$ with initial position (1,0) and initial coin state $|0\rangle_3$. The time step is taken up to 300. The generic depolarizer gate noise and amplitude damping idle noise is incorporated in the circuit. The error parameters are chosen from uniform distribution. Specifically, in (a), $C \in \mathcal{X}_\theta, \theta = \pi$ i.e. the coin is the Grover matrix. In (b), $C \in \mathcal{Y}_\theta, \theta = \pi/2$. In (c), $C \in \mathcal{Z}_\theta, \theta = \pi/3$. In subfigure (d), $C \in \mathcal{W}_\theta, \theta = -\pi/4$. The y axis of the plot is in log scale.

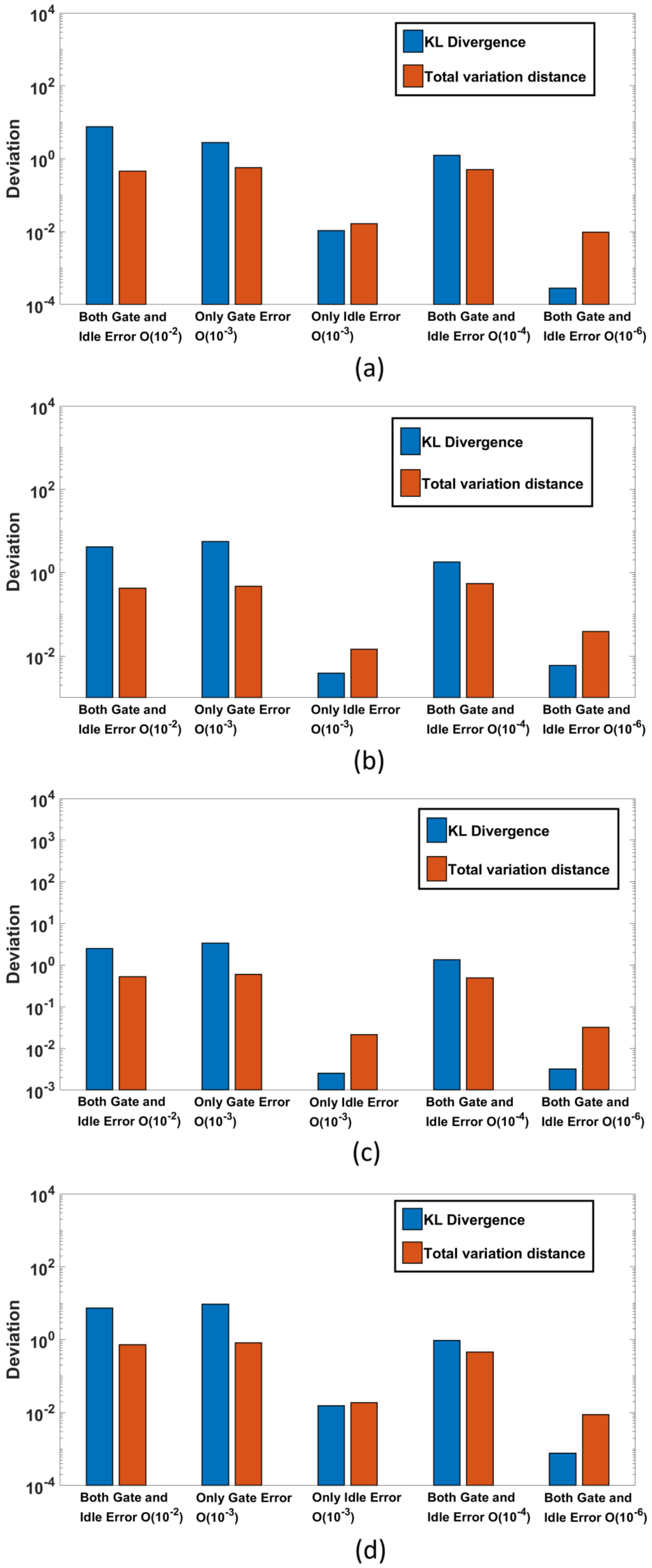

FIG. 7. Comparison $D_{\mathrm{KL}}(\text{IDEAL}\|\text{NOISY})$ (left blue bar) and $TVD(\text{IDEAL}\|\text{NOISY})$ (right orange bar) between the time-averaged probability distributions obtained through noiseless and noisy circuits for DTQWs in $\mathrm{Cay}(D_{27}, \{\mu, \xi\})$ taking coins (denoted by C) from the classes , $\mathcal{X}_\theta, \mathcal{Y}_\theta, \mathcal{Z}_\theta, \mathcal{W}_\theta$ with initial position (1,0) and initial coin state $|0\rangle_3$. The time step is taken up to 300. The generic depolarizer gate noise and phase damping idle noise is incorporated in the circuit and the error parameters are chosen from uniform distribution. Specifically, in (a), $C \in \mathcal{X}_\theta, \theta = \pi$, i.e., the coin is the Grover matrix. In (b), $C \in \mathcal{Y}_\theta, \theta = \pi/2$. In (c), $C \in \mathcal{Z}_\theta, \theta = \pi/3$. In subfigure (d), $C \in \mathcal{W}_\theta, \theta = -\pi/4$. The y axis of the plot is in log scale.

effect of gate noise is further emphasized from the third and fourth bars and columns in the figure where we see that a small gate error coupled with a small idle error provides a more noisy distribution as compared to a distribution obtained via a larger idle error with no gate error. Further, comparing second and third columns in the Fig. 6 is another justification that gate errors are more significant than idle errors. Now, in Fig. 7 we plot same comparison between noisy and noiseless distributions using KL divergence and TVD. Though, the idle error comprises of phase damping instead of amplitude damping in this case, the results observed are found to be similar to that mentioned in Fig. 6 as well.

It is also to be noted that the y-axis plots (deviation) in figures involving KL divergence and TVD have been carried out in log scale, i.e., we are also interested in measuring the order of deviation as well from our results. We have incorporated this log scale due the fact that the values of KL divergence and TVD becomes extremely small when the gate and idle error of order $O(10^{-6})$ or less. In other words, $D_{\mathrm{KL}}(\text{IDEAL}\|\text{NOISY})$ and $TVD(\text{IDEAL}\|\text{NOISY})$ where the noise $O(10^{-6})$ or less becomes extremely difficult to track in normal scale due to its very small values as compared to the cases when the noise is greater than $O(10^{-6})$.

Similar results comparing noisy and noiseless time-averaged probability distributions are obtained for DTQWs on $\mathrm{Cay}(\mathbb{Z}_{27}, \{1, -1\})$. In Figs. 8 and 9 we plot the KL divergence $D_{\mathrm{KL}}(\text{IDEAL}\|\text{NOISY})$ and the total variation distance $TVD(\text{IDEAL}\|\text{NOISY})$ between the noiseless and noisy time-averaged probability distributions for finding the walker over the vertices of $\mathrm{Cay}(\mathbb{Z}_{27}, \{1, -1\})$ for the initial coin state $\frac{1}{\sqrt{3}}(|0\rangle_3 + |1\rangle_3 + |2\rangle_3)$ and starting vertex 0. Several coins from classes $\mathcal{X}_\theta, \mathcal{Y}_\theta, \mathcal{W}_\theta, \mathcal{Z}_\theta$ are chosen similar to Fig. 6 and Fig. 7. The generic depolarizer gate noise is considered along with amplitude damping (Fig. 8) and phase damping (Fig. 9).

Hence, in our proposed circuit when incorporated with both gate and idle errors of order $O(10^{-6})$ or less behaves almost similar to its noiseless counterpart as seen from the values of KL divergence and TVD in Figs. 6–9.

VI. CONCLUSION

In this paper we develop qutrit quantum circuit models for quantum walks on Cayley graphs of dihedral groups and additive group of integers modulo a positive integer. The circuits are based on elementary qutrit gates, and during the process we propose qutrit quantum circuit models for block-diagonal special unitary matrices of order 3^n with diagonal blocks as special unitary matrices of order three. We derive the circuit complexity of the developed circuit models and we numerically simulate the time-averaged probability distributions of the walker employing the circuit models with various noise models. These results show that gate noises significantly impact the distributions of noiseless models compared to

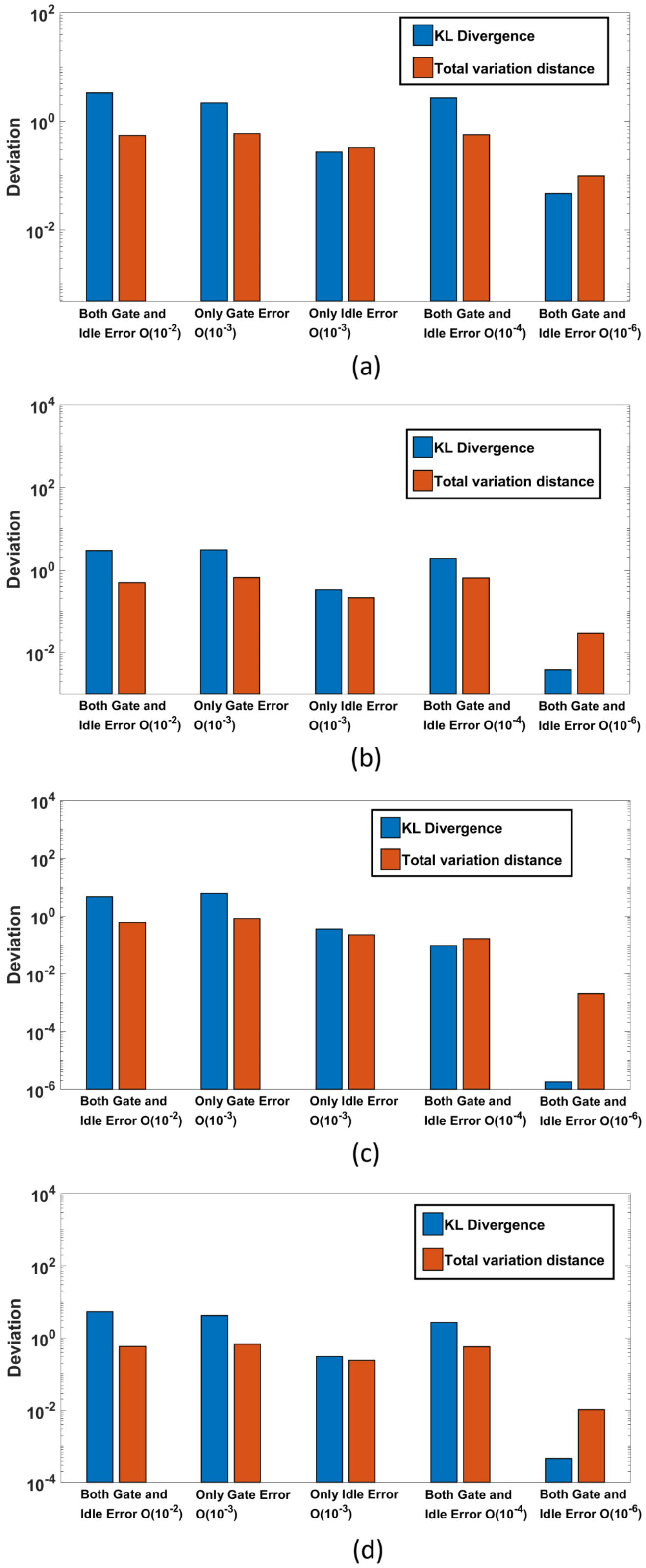

FIG. 8. Comparison $D_{\mathrm{KL}}(\mathrm{IDEAL}\|\mathrm{NOISY})$ (left blue bar) and $TVD(\mathrm{IDEAL}\|\mathrm{NOISY})$ (right orange bar) between the time-averaged probability distributions obtained through noiseless and noisy circuits for DTQWs in $\mathrm{Cay}(\mathbb{Z}_{27}, \{1, -1\})$ taking coins (denoted by C) from the classes , $\mathcal{X}_\theta, \mathcal{Y}_\theta, \mathcal{Z}_\theta, \mathcal{W}_\theta$ with initial position 0 and initial coin state $\frac{1}{\sqrt{3}}(|0\rangle_3 + |1\rangle_3 + |2\rangle_3)$. The time step is taken up to 300. The generic depolarizer gate noise and amplitude damping idle noise is incorporated in the circuit. The error parameters are chosen from uniform distribution. Specifically, in (a), $C \in \mathcal{X}_\theta, \theta = \pi$, i.e., the coin is the Grover matrix. In (b), $C \in \mathcal{Y}_\theta, \theta = \pi/2$. In (c), $C \in \mathcal{Z}_\theta, \theta = \pi/3$. In (d), $C \in \mathcal{W}_\theta, \theta = -\pi/4$. The y axis of the plot is in log scale.

amplitude or phase damping errors. We observe that our noisy circuit behaves very close to its noiseless counterpart if the gate and idle errors are set to be not more than $O(10^{-6})$.

ACKNOWLEDGMENTS

R.S.S. acknowledges support through Prime Minister's Research Fellowship (PMRF), Government of India. We express our gratitude to the reviewers for their insightful comments, which have greatly improved the manuscript.

APPENDIX A: PROOF OF THEOREM 1

Proof. Since any 3×3 unitary matrix is a single-qutrit gate, let the matrix be $C = \begin{bmatrix} c_{11} & c_{12} & c_{13} \\ c_{21} & c_{22} & c_{23} \\ c_{31} & c_{32} & c_{33} \end{bmatrix} \in \mathrm{SU}(3)$ such that each c_{ij} is of the form $r_{ij}e^{-i\alpha_{ij}}$ where $r_{ij} \geqslant 0$ and $\alpha_{ij} \in \mathbb{R}$. We choose C to be special unitary due to the fact that any unitary matrix is a special unitary matrix multiplied by a global phase. Hence, by left multiplying the matrix $M_1 = \frac{1}{\sqrt{r_{11}^2+r_{31}^2}} \begin{bmatrix} r_{11}e^{i\alpha_{11}} & 0 & r_{31}e^{i\alpha_{31}} \\ 0 & 1 & 0 \\ -r_{31}e^{-i\alpha_{31}} & 0 & r_{11}e^{-i\alpha_{11}} \end{bmatrix}$ to C, we obtain $M_1C = \begin{bmatrix} \sqrt{r_{11}^2 + r_{31}^2} & \times & \times \\ c_{21} & \times & \times \\ 0 & \times & \times \end{bmatrix}$. It is of note that M_1 can be written as $M_1 := M_1(\theta_1, \phi_1, \psi_1) = \begin{bmatrix} \cos\theta_1 e^{i\phi_1} & 0 & \sin\theta_1 e^{i\psi_1} \\ 0 & 1 & 0 \\ -\sin\theta_1 e^{-i\psi_1} & 0 & \cos\theta_1 e^{-i\phi_1} \end{bmatrix}$ where $\theta_1 = \arctan\frac{r_{31}}{r_{11}}$, $\phi_1 = \alpha_{11}$, $\psi_1 = \alpha_{31}$. Also, from ZYZ decomposition [49],

$$M_1(\theta_1, \phi_1, \psi_1) = R_{Z02}\left(\frac{\phi_1 + \psi_1}{2}\right) R_{Y02}(\theta_1) R_{Z02}\left(\frac{\phi_1 - \psi_1}{2}\right). \tag{A1}$$

Similarly, left multiplying the matrix M_1C by the matrix $M_2 = \frac{1}{\sqrt{r_{11}^2+r_{21}^2+r_{31}^2}} \begin{bmatrix} \sqrt{r_{11}^2 + r_{21}^2} & r_{21}e^{i\alpha_{21}} & 0 \\ -r_{21}e^{-i\alpha_{21}} & \sqrt{r_{11}^2 + r_{21}^2} & 0 \\ 0 & 0 & 1 \end{bmatrix}$, we obtain

$$M_2M_1C = \begin{bmatrix} \sqrt{r_{11}^2 + r_{21}^2 + r_{31}^2} & \times & \times \\ 0 & \times & \times \\ 0 & \times & \times \end{bmatrix} = \begin{bmatrix} 1 & \times & \times \\ 0 & \times & \times \\ 0 & \times & \times \end{bmatrix}$$

since $|c_{11}|^2 + |c_{21}|^2 + |c_{31}|^2 = 1$ and similarly, $M_2 := M_2(\theta_2, \phi_2, \psi_2) = \begin{bmatrix} \cos\theta_2 e^{i\phi_2} & \sin\theta_2 e^{i\psi_2} & 0 \\ -\sin\theta_2 e^{-i\psi_2} & \cos\theta_2 e^{-i\phi_2} & 0 \\ 0 & 0 & 1 \end{bmatrix}$ where $\theta_2 = \arctan\frac{\sqrt{r_{11}^2+r_{31}^2}}{r_{21}}$, $\phi_2 = 0$, $\psi_2 = \alpha_{21}$, i.e., we obtain

$M_2(\theta_2, 0, \psi_2)$. Further from, ZYZ decomposition again, we have

$$M_2(\theta_2, 0, \psi_2) = R_{Z01}\left(\frac{\psi_2}{2}\right)R_{Y01}(\theta_2)R_{Z01}\left(\frac{-\psi_2}{2}\right). \quad \text{(A2)}$$

Continuing in this way, we see that there exists $M_3 = M_3(\theta_3, \phi_3, \psi_3) = \begin{bmatrix} 1 & 0 & 0 \\ 0 & \cos\theta_3 e^{i\phi_3} & \sin\theta_3 e^{i\psi_3} \\ 0 & -\sin\theta_3 e^{-i\psi_3} & \cos\theta_3 e^{-i\phi_3} \end{bmatrix}$ such that $M_3M_2M_1C = \underbrace{\begin{bmatrix} 1 & \times & \times \\ 0 & r & \times \\ 0 & 0 & \times \end{bmatrix}}_{R}$ where $r > 0$.

Clearly, R is an upper triangular matrix, which is also a special unitary matrix. Hence, R is a special unitary diagonal matrix. Further, since two diagonal entries of R are real and positive, hence entries in R cannot be complex on account of the determinant being 1. Hence $R = I$, i.e., the identity matrix. We also have

$$M_3(\theta_3, \phi_3, \psi_3) = R_{Z12}\left(\frac{\phi_3 + \psi_3}{2}\right)R_{Y12}(\theta_3)R_{Z12}\left(\frac{\phi_3 - \psi_3}{2}\right). \quad \text{(A3)}$$

Hence, $M_3(\theta_3, \phi_3, \psi_3)M_2(\theta_2, 0, \psi_2)M_1(\theta_1, \phi_1, \psi_1)C = I$. Thus, we obtain

$$\begin{aligned} C &= M_1^*(\theta_1, \phi_1, \psi_1)M_2^*(\theta_2, 0, \psi_2)M_1(\theta_1, \phi_1, \psi_1) \\ &\quad \times M_3^*(\theta_3, \phi_3, \psi_3) \\ &= M_1(-\theta_1, -\phi_1, \psi_1)M_2(-\theta_2, 0, \psi_2)M_3(-\theta_3, -\phi_3, \psi_3) \end{aligned} \quad \text{(A4)}$$

for any arbitrary $C \in SU(3)$. From this discussion, the proof follows immediately. ■

APPENDIX B: PROOF OF THEOREM 2

Proof. Let $N = 3^n$. Then from the construction of U_{circ}, we see that any state of the form $|l\rangle_3 |2\rangle_3 |r_n\rangle_3 \dots |r_1\rangle_3$, i.e., any state with $|2\rangle_3$ in the reflection state remains invariant to the circuit where the coin state $|l\rangle_3 \in \{|0\rangle_3, |1\rangle_3, |2\rangle_3\}$, and $0 \leqslant r \leqslant N-1$ such that $r = \sum_{j=1}^{n} r_j 3^{j-1}$, $r_j \in \{0, 1, 2\}$, $j \in \{1, \dots, n\}$. For the state $|l\rangle_3 |s\rangle_3 |r_n\rangle_3 \dots |r_1\rangle_3$, $s \in \{0, 1\}$, $r_j \in \{0, 1, 2\}$, $j \in \{1, \dots, n\}$, the circuit acts nontrivially.

Then, the state of the walker after time t is given by $|\phi(t)\rangle = U_{\text{circ}}^t |\phi(0)\rangle$ for initial state $|\phi(0)\rangle$. Further

$$\begin{aligned} |\phi(t)\rangle &= \sum_{s=0}^{2}\sum_{r=0}^{N-1}\sum_{l\in\{0,1,2\}} \phi(l, s, r, t)\,|l\rangle \otimes |s\rangle_3 |r_n\rangle_3 \dots |r_1\rangle_3 \\ &= \sum_{r=0}^{N-1} |\phi(r, t)\rangle \otimes |r_n\rangle_3 \dots |r_1\rangle_3, \end{aligned}$$

where $\sum_{s=0}^{2}\sum_{r=0}^{N-1} |\phi(l, s, r, t)|^2 = 1$ and $r = \sum_{j=1}^{n} r_j 3^{j-1}$, $r_j \in \{0, 1, 2\}$, $j \in \{1, \dots, n\}$. Further $|\phi(r, t)\rangle = [\phi(0, 0, r, t)$ $\phi(0, 1, r, t)$ $\phi(0, 2, r, t)$ $\phi(1, 0, r, t)$ $\phi(1, 1, r, t)$ $\phi(1, 2, r, t)$

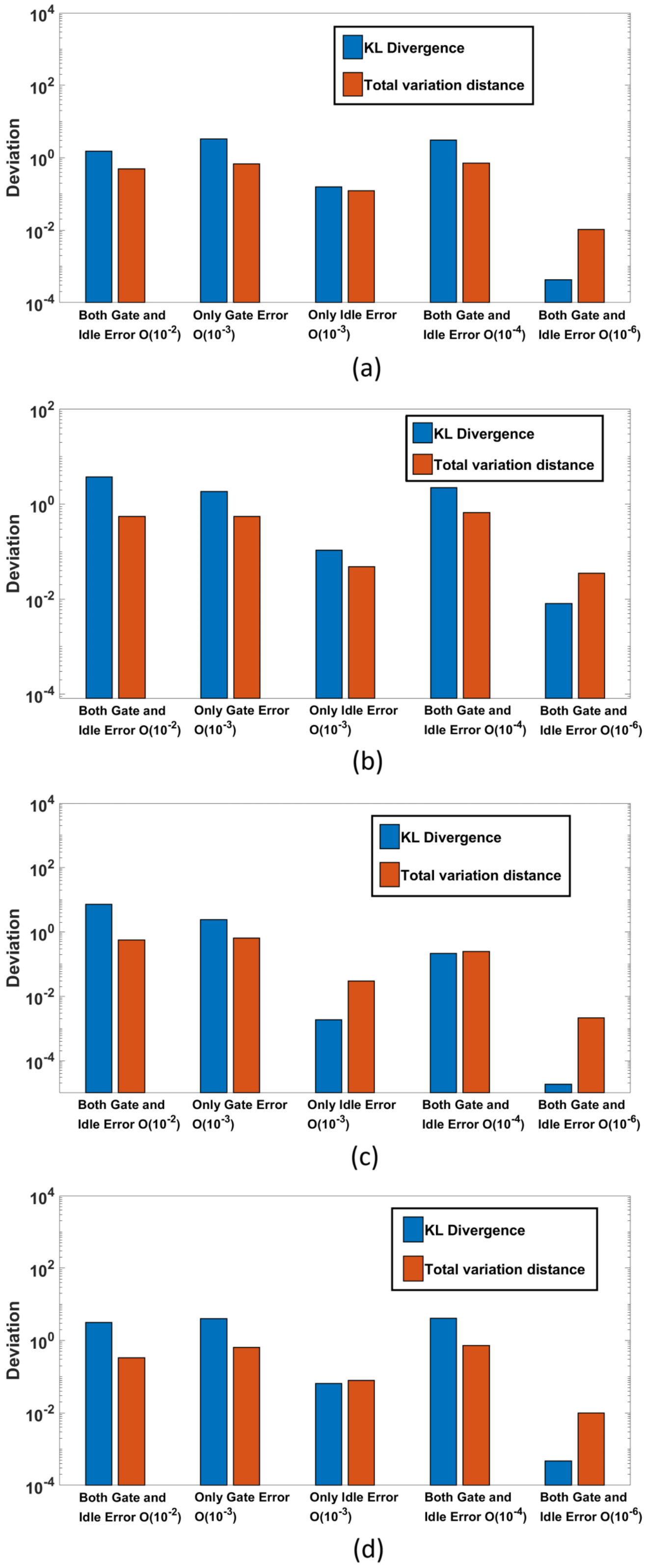

FIG. 9. Comparison $D_{\text{KL}}(\text{IDEAL}\|\text{NOISY})$ and $TVD(\text{IDEAL}\|\text{NOISY})$ between the time-averaged probability distributions obtained through noiseless and noisy circuits for DTQWs in $\text{Cay}(\mathbb{Z}_{27}, \{1, -1\})$ taking coins from the classes , $\mathcal{X}_\theta, \mathcal{Y}_\theta, \mathcal{Z}_\theta, \mathcal{W}_\theta$ with initial position 0 and initial coin state $\frac{1}{\sqrt{3}}(|0\rangle_3 + |1\rangle_3 + |2\rangle_3)$. The time step is taken up to 300. The generic depolarizer gate noise and phase damping idle noise is incorporated in the circuit and the error parameters are chosen from uniform distribution. Specifically, in (a), $C \in \mathcal{X}_\theta, \theta = \pi$, i.e., the coin is the Grover matrix. In (b), $C \in \mathcal{Y}_\theta, \theta = \pi/2$. In (c), $C \in \mathcal{Z}_\theta, \theta = \pi/3$. In (d), $C \in \mathcal{W}_\theta, \theta = -\pi/4$. The y axis of the plot is in log scale.

$\phi(2,0,r,t) \quad \phi(2,1,r,t) \quad \phi(2,2,r,t)]'$ where $'$ denotes the conjugate-transpose operation. If the coin operator is $C = [c_{ij}] \in \mathbb{C}^{3\times 3}$ then the probability that the walker will be at the vertex labeled (s, r) at time t is $\sum_{l=0,1,2} |\phi(l, s, r, t)|^2$, where $s \in \{0, 1\}$. Further, the state $|l\rangle_3 \, |2\rangle_3 \, |r_n\rangle_3 \ldots |r_1\rangle_3$ is invariant in our circuit for all $0 \leqslant r \leqslant N-1, 0 \leqslant l \leqslant 2$. Thus it is computationally easy to verify that

$$|\phi(r, t+1)\rangle = V_1 \, |\phi(r-1, t)\rangle + V_2 \, |\phi(r+1, t)\rangle + V_3 \, |\phi(r, t)\rangle \,,$$

where

$$V_1 = \begin{bmatrix} c_{11} & 0 & 0 & c_{12} & 0 & 0 & c_{13} & 0 & 0 \\ 0 & 0 & 0 & 0 & 0 & 0 & 0 & 0 & 0 \\ 0 & 0 & 0 & 0 & 0 & 0 & 0 & 0 & 0 \\ 0 & 0 & 0 & 0 & 0 & 0 & 0 & 0 & 0 \\ 0 & 0 & 0 & 0 & 0 & 0 & 0 & 0 & 0 \\ 0 & 0 & 0 & 0 & 0 & 0 & 0 & 0 & 0 \\ 0 & 0 & 0 & 0 & 0 & 0 & 0 & 0 & 0 \\ 0 & 0 & 0 & 0 & 0 & 0 & 0 & 0 & 0 \\ 0 & 0 & 0 & 0 & 0 & 0 & 0 & 0 & 0 \end{bmatrix}, \quad V_2 = \begin{bmatrix} 0 & 0 & 0 & 0 & 0 & 0 & 0 & 0 & 0 \\ 0 & c_{11} & 0 & 0 & c_{12} & 0 & 0 & c_{13} & 0 \\ 0 & 0 & 0 & 0 & 0 & 0 & 0 & 0 & 0 \\ 0 & 0 & 0 & 0 & 0 & 0 & 0 & 0 & 0 \\ 0 & 0 & 0 & 0 & 0 & 0 & 0 & 0 & 0 \\ 0 & 0 & 0 & 0 & 0 & 0 & 0 & 0 & 0 \\ 0 & 0 & 0 & 0 & 0 & 0 & 0 & 0 & 0 \\ 0 & 0 & 0 & 0 & 0 & 0 & 0 & 0 & 0 \\ 0 & 0 & 0 & 0 & 0 & 0 & 0 & 0 & 0 \end{bmatrix},$$

$$V_3 = \begin{bmatrix} 0 & 0 & 0 & 0 & 0 & 0 & 0 & 0 & 0 \\ 0 & 0 & 0 & 0 & 0 & 0 & 0 & 0 & 0 \\ 0 & 0 & 1 & 0 & 0 & 0 & 0 & 0 & 0 \\ c_{21} & 0 & 0 & c_{22} & 0 & 0 & c_{23} & 0 & 0 \\ 0 & c_{21} & 0 & 0 & c_{22} & 0 & 0 & c_{23} & 0 \\ 0 & 0 & 0 & 0 & 0 & 1 & 0 & 0 & 0 \\ 0 & c_{31} & 0 & 0 & c_{32} & 0 & 0 & c_{33} & 0 \\ c_{31} & 0 & 0 & c_{32} & 0 & 0 & c_{32} & 0 & 0 \\ 0 & 0 & 0 & 0 & 0 & 0 & 0 & 0 & 1 \end{bmatrix}.$$

Further, using the discrete Fourier (DFT) transformation [54] of $|\phi(r,t)\rangle$, we get $|\Phi(k,t)\rangle = \sum_{r=0}^{N-1} e^{-i2\pi kr/N} \, |\phi(r,t)\rangle$ where $0 \leqslant k \leqslant N-1$. Hence, we obtain $|(\Phi(k,t+1))\rangle = \sum_{r=0}^{N-1} e^{-i2\pi kr/N} V_1 \, |(\phi(r+1,t))\rangle + \sum_{r=0}^{N-1} e^{-i2\pi kr/N} V_2 \, |[\phi(r-1,t)]\rangle + \sum_{r=0}^{N-1} e^{-i2\pi kr/N} V_3 \, |[\phi(r,t)]\rangle$. Consequently, we obtain the Fourier evolution matrix $|(\Phi[k,t+1)]\rangle = U_{\text{circ}}(k) \, |\Phi(k,t)\rangle$ where

$$U_{\text{circ}}(k) = \begin{bmatrix} c_{11}e^{-2i\pi k/N} & 0 & 0 & c_{12}e^{-2i\pi k/N} & 0 & 0 & c_{13}e^{-2i\pi k/N} & 0 & 0 \\ 0 & c_{11}e^{2i\pi k/N} & 0 & 0 & c_{12}e^{2i\pi k/N} & 0 & 0 & c_{13}e^{2i\pi k/N} & 0 \\ 0 & 0 & 1 & 0 & 0 & 0 & 0 & 0 & 0 \\ c_{21} & 0 & 0 & c_{22} & 0 & 0 & c_{23} & 0 & 0 \\ 0 & c_{21} & 0 & 0 & c_{22} & 0 & 0 & c_{23} & 0 \\ 0 & 0 & 0 & 0 & 0 & 1 & 0 & 0 & 0 \\ 0 & c_{31} & 0 & 0 & c_{32} & 0 & 0 & c_{33} & 0 \\ c_{31} & 0 & 0 & c_{32} & 0 & 0 & c_{32} & 0 & 0 \\ 0 & 0 & 0 & 0 & 0 & 0 & 0 & 0 & 1 \end{bmatrix}.$$

From elementary computation, we observe that $U_{circ}(k) = P[\begin{array}{c|c} U_{\text{Cay}(D_N)}(k) & 0 \\ \hline 0 & I_3 \end{array}]P^T$ holds true for all $k \in \{0, 1, \ldots, N-1\}$ where P is a 9×9 permutation matrix such that $P = P_{(34)}P_{(45)}P_{(57)}P_{(68)}$, and $U_{\text{Cay}(D_N)}(k) \in \mathbb{C}^{6\times 6}$ is the Fourier evolution matrix of $U_{\text{Cay}(D_N)}$ (see [12]). Note that $P_{(a,b)}$ denotes a transposition matrix i.e. an identity matrix whose a and b-th rows are interchanged. From Theorem 2.1 in Ref. [12], we know that the spectra of $U_{\text{circ}}(k)$ and $U_{\text{Cay}(D_N)}(k)$, $0 \leqslant k \leqslant N-1$ are equal to that of U_{circ} and $U_{\text{Cay}(D_N)}$, respectively. Hence, we obtain

$$U_{\text{circ}} = (P \otimes I_{3^n}) \left[\begin{array}{c|c} U_{\text{Cay}(D_N)_{6.3^n \times 6.3^n}} & 0 \\ \hline 0 & I_{3^{n+2} - 6.3^n} \end{array} \right] (P \otimes I_{3^n})^T = (P \otimes I_{3^n}) \left[\begin{array}{c|c} U_{\text{Cay}(D_N)_{6.3^n \times 6.3^n}} & 0 \\ \hline 0 & I_{3^{n+1}} \end{array} \right] (P \otimes I_{3^n})^T .$$

This concludes the proof for $N = 3^n$. Next, consider $3^{n-1} \leqslant N < 3^n$. Then the additional states such as $|l\rangle_3 \, |s\rangle_3 \, |r'_n\rangle_3 \ldots |r'_1\rangle_3$ are unaffected in the circuit where $s \in \{0, 1\}$ and $r'_j \in \{0, 1, 2\}$ such that $\sum_{j=1}^{n} r'_j 3^{j-1} > N$. The rest of the proof is similar to the first case and after a bit of computations we obtain

$$U_{\text{circ}} = (P \otimes I_{3^n}) \left[\begin{array}{c|c|c} U_{\text{Cay}(D_N)_{6N \times 6N}} & 0 & 0 \\ \hline 0 & I_{6.3^n - 6N} & 0 \\ \hline 0 & 0 & I_{3^{n+2} - 6N} \end{array} \right] (P \otimes I_{3^n})^T .$$

This completes the proof. ■

APPENDIX C: PROOF OF LEMMA 1

Proof. We will prove the theorem for the first case. The proofs for the rest of the cases and statements are similar. For the first case, the unitary matrix corresponding to the circuit in Eq. (31) is given by

$$\left(I_3\otimes\left[\begin{array}{c|c|c} R_{Y01}(\theta_1) & 0 & 0\\ \hline 0 & \ddots & 0\\ \hline 0 & 0 & R_{Y01}(\theta_{3^{n-2}})\end{array}\right]\right)\left[\begin{array}{c|c|c} I_{3^{n-2}} & O & O\\ \hline O & U & O\\ \hline O & O & I_{3^{n-2}}\end{array}\right]\left(I_3\otimes\left[\begin{array}{c|c|c} R_{Y01}(\phi_1) & 0 & 0\\ \hline 0 & \ddots & 0\\ \hline 0 & 0 & R_{Y01}(\phi_{3^{n-2}})\end{array}\right]\right)$$

$$\left[\begin{array}{c|c|c} I_{3^{n-2}} & O & O\\ \hline O & U & O\\ \hline O & O & I_{3^{n-2}}\end{array}\right]\left[\begin{array}{c|c|c} I_{3^{n-2}} & O & O\\ \hline O & I_{3^{n-2}} & O\\ \hline O & O & U\end{array}\right]\left(I_3\otimes\left[\begin{array}{c|c|c} R_{Y01}(\gamma_1) & 0 & 0\\ \hline 0 & \ddots & 0\\ \hline 0 & 0 & R_{Y01}(\gamma_{3^{n-2}})\end{array}\right]\right)\left[\begin{array}{c|c|c} I_{3^{n-2}} & O & O\\ \hline O & I_{3^{n-2}} & O\\ \hline O & O & U\end{array}\right]$$

where $U_{3^{n-2}\times 3^{n-2}}=\left[\begin{array}{c|c|c|c} X_{0,1} & 0 & 0 & 0\\ \hline 0 & X_{0,1} & 0 & 0\\ \hline 0 & 0 & \ddots & 0\\ \hline 0 & 0 & 0 & X_{0,1}\end{array}\right]$. This gives the matrix $\left[\begin{array}{c|c|c} R_{11} & 0 & 0\\ \hline 0 & R_{22} & 0\\ \hline 0 & 0 & R_{33}\end{array}\right]$ where

$$R_{11}=\left[\begin{array}{c|c|c} R_{Y01}(\theta_1+\phi_1+\gamma_1) & 0 & 0\\ \hline 0 & \ddots & 0\\ \hline 0 & 0 & R_{Y01}(\theta_{3^{n-2}}+\phi_{3^{n-2}}+\gamma_{3^{n-2}})\end{array}\right]$$

$$R_{22}=\left[\begin{array}{c|c|c} X_{0,1}R_{Y01}(\phi_1)X_{0,1}R_{Y1}(\theta_1+\gamma_1) & 0 & 0\\ \hline 0 & \ddots & 0\\ \hline 0 & 0 & X_{0,1}R_{Y01}(\phi_{3^{n-2}})X_{0,1}R_{Y01}(\theta_{3^{n-2}}+\gamma_{3^{n-2}})\end{array}\right]$$

$$=\left[\begin{array}{c|c|c} R_{Y01}(\theta_1-\phi_1+\gamma_1) & 0 & 0\\ \hline 0 & \ddots & 0\\ \hline 0 & 0 & R_{Y01}(\theta_{3^{n-2}}-\phi_{3^{n-2}}+\gamma_{3^{n-2}})\end{array}\right].$$

$$R_{33}=\left[\begin{array}{c|c|c} X_{0,1}R_{Y01}(\gamma_1)X_{0,1}R_{Y01}(\theta_1+\phi_1) & 0 & 0\\ \hline 0 & \ddots & 0\\ \hline 0 & 0 & X_{0,1}R_{Y01}(\gamma_{3^{n-2}})X_{0,1}R_{Y01}(\theta_{3^{n-2}}+\phi_{3^{n-2}})\end{array}\right]$$

$$=\left[\begin{array}{c|c|c} R_{Y01}(\theta_1+\phi_1-\gamma_1) & 0 & 0\\ \hline 0 & \ddots & 0\\ \hline 0 & 0 & R_{Y01}(\theta_{3^{n-2}}+\phi_{3^{n-2}}-\gamma_{3^{n-2}})\end{array}\right].$$

This completes the proof. The proof of the other statements and cases follow similarly. ■

---

[1] D. Aharonov, A. Ambainis, J. Kempe, and U. Vazirani, Quantum walks on graphs, in *Proceedings of the Thirty-Third Annual ACM Symposium on Theory of Computing* (Association for Computing Machinery, New York, 2001), pp. 50–59.

[2] A. M. Childs, Universal computation by quantum walk, Phys. Rev. Lett. **102**, 180501 (2009).

[3] A. M. Childs, D. Gosset, and Z. Webb, Universal computation by multiparticle quantum walk, Science **339**, 791 (2013).

[4] N. B. Lovett, S. Cooper, M. Everitt, M. Trevers, and V. Kendon, Universal quantum computation using the discrete-time quantum walk, Phys. Rev. A **81**, 042330 (2010).

[5] A. M. Childs, E. Farhi, S. Gutmann, An example of the difference between quantum and classical random walks, Quantum Info. Proc. **1**, 35 (2002).

[6] S. E. Venegas-Andraca, Quantum walks: A comprehensive review, Quantum Inf. Process. **11**, 1015 (2012).

[7] A. Banerjee, Discrete quantum walks on the symmetric group, Quantum Stud. Math. Found. (2024), doi:10.1007/s40509-024-00332-9.

[8] N. Inui, Y. Konishi, and N. Konno, Localization of two-dimensional quantum walks, Phys. Rev. A **69**, 052323 (2004).

[9] T. Kajiwara, N. Konno, S. Koyama, K. Saito, Periodicity for the 3-state quantum walk on cycles, arXiv:1907.01725.

[10] S. Kubota, H. Sekido, H. Yata, Periodicity of quantum walks defined by mixed paths and mixed cycles, Linear Algebra Appl. **630**, 15 (2021).

[11] Y. Liu, J. Yuan, W. Dai, D. Li, Three-state quantum walk on the Cayley graph of the dihedral group, Quantum Info. Proc. **20**, 106 (2021).

[12] R. S. Sarkar and B. Adhikari, Discrete-time quantum walks on Cayley graphs of Dihedral groups using generalized Grover coins, Quantum Info. Proc. **23**, 172 (2024).

[13] A. Bisio, G. M. D'Ariano, M. Erba, P. Perinotti, and A. Tosini, Quantum walks with a one-dimensional coin, Phys. Rev. A **93**, 062334 (2016).

[14] G. M. D'Ariano, M. Erba, and P. Perinotti, Chirality from quantum walks without a quantum coin, Phys. Rev. A **100**, 012105 (2019).

[15] J. Kempe, Quantum random walks: An introductory overview, Contemp. Phys. **44**, 307 (2003).

[16] Z. Yan, Y. R. Zhang, M. Gong, Y. Wu, Y. Zheng, S. Li, C. Wang, F. Liang, J. Lin, Y. Xu, C. Guo, L. Sun, C. Z. Peng, K. Xia, H. Deng, H. Rong, J. Q. You, F. Nori, H. Fan, X. Zhu, and J. W. Pan, Strongly correlated quantum walks with a 12-qubit superconducting processor, Science **364**, 753 (2019).

[17] C. Huerta Alderete, S. Singh, N. H. Nguyen *et al.*, Quantum walks and Dirac cellular automata on a programmable trapped-ion quantum computer, Nat. Commun. **11**, 3720 (2020).

[18] F. Acasiete, F. P. Agostini, J. K. Moqadam *et al.*, Implementation of quantum walks on IBM quantum computers, Quantum Info. Proc. **19**, 426 (2020).

[19] R. Balu, D. Castillo, and G. Siopsis, Physical realization of topological quantum walks on IBM-Q and beyond, Quantum Sci. Technol. **3**, 035001 (2018).

[20] S. Singh, C. H. Alderete, R. Balu, C. Monroe, N. M. Linke, and C. M. Chandrashekar, Quantum circuits for the realization of equivalent forms of one-dimensional discrete-time quantum walks on near-term quantum hardware, Phys. Rev. A **104**, 062401 (2021).

[21] J. Q. Zhou, L. Cai, Q. P. Su, and C. P. Yang, Protocol of a quantum walk in circuit QED, Phys. Rev. A **100**, 012343 (2019).

[22] P. Gokhale, J. M. Baker, C. Duckering, N. C. Brown, K. R. Brown, and F. T. Chong, Asymptotic improvements to quantum circuits via qutrits, in *Proceedings of the 46th International Symposium on Computer Architecture* (Association for Computing Machinery, ISCA '19, 2019), pp. 554–566.

[23] P. Gokhale, J. M. Baker, C. Duckering, F. T. Chong, N. C. Brown, and K. R. Brown, Extending the frontier of quantum computers with qutrits, IEEE Micro **40**, 64 (2020).

[24] R. Majumdar, A. Saha, A. Chakrabarti, and S. Sur-Kolay, On fault tolerance of circuits with intermediate qutrit-assisted gate decomposition, arXiv:2212.07866.

[25] E. T. Campbell, Enhanced fault-tolerant quantum computing in d-level systems, Phys. Rev. Lett. **113**, 230501 (2014).

[26] S. Muralidharan, C. L. Zou, L. Li, J. Wen, L. Jiang, Overcoming erasure errors with multilevel systems, New J. Phys. **19**, 013026 (2017).

[27] E. T. Campbell, H. Anwar, and D. E. Browne, Magic-state distillation in all prime dimensions using quantum reed-muller codes, Phys. Rev. X **2**, 041021 (2012).

[28] H. Bechmann-Pasquinucci, and A. Peres, Quantum cryptography with 3-state systems, Phys. Rev. Lett. **85**, 3313 (2000).

[29] D. Bruß, and C. Macchiavello, Optimal eavesdropping in cryptography with three-dimensional quantum states, Phys. Rev. Lett. **88**, 127901 (2002).

[30] A. Vaziri, G. Weihs, and A. Zeilinger, Experimental two-photon, three-dimensional entanglement for quantum communication, Phys. Rev. Lett. **89**, 240401 (2002).

[31] A. Morvan, V. V. Ramasesh, M. S. Blok, J. M. Kreikebaum, K. O'Brien, L. Chen, B. K. Mitchell, R. K. Naik, D. I. Santiago, and I. Siddiqi, Qutrit randomized benchmarking, Phys. Rev. Lett. **126**, 210504 (2021).

[32] B. L. Douglas, and J. B. Wang, Efficient quantum circuit implementation of quantum walks, Phys. Rev. A **79**, 052335 (2009).

[33] A. Saha, S. B. Mandal, D. Saha, and A. Chakrabarti, One-dimensional lazy quantum walk in ternary system, IEEE Trans. Quantum Eng. **2**, 3102012 (2021).

[34] A. Saha, D. Saha, and A. Chakrabarti, Discrete-time quantum walks in qudit systems, arXiv:2207.04319.

[35] A. Bocharov, S. X. Cui, M. Roetteler, and K. M. Svore, Improved quantum ternary arithmetics, Quantum Inf. Comput. **16**, 862 (2016).

[36] A. Bocharov, M. Roetteler, and K. M. Svore, Factoring with qutrits: Shor's algorithm on ternary and metaplectic quantum architectures, Phys. Rev. A **96**, 012306 (2017).

[37] Y. Fan, A generalization of the Deutsch-Jozsa algorithm to multi-valued quantum logic, in *Proceedings of 37th International Symposium on Multiple-Valued Logic (ISMVL'07, 2007)*, p. 12.

[38] G. Bottrill, M. Pandey, and O. Di Matteo, Exploring the potential of qutrits for quantum optimization of graph coloring, in *2023 IEEE International Conference on Quantum Computing and Engineering* (QCE, Bellevue, 2023), pp. 177–183.

[39] Y. M. Di, and H. R. Wei, Synthesis of multivalued quantum logic circuits by elementary gates, Phys. Rev. A **87**, 012325 (2013).

[40] P. Sadowski, J. A. Miszczak, and M. Ostaszewski, Lively quantum walks on cycles, J. Phys. A: Math. Theor. **49**, 375302 (2016).

[41] R. S. Sarkar, A. Mandal, and B. Adhikari, Periodicity of lively quantum walks on cycles with generalized Grover coin, Linear Algebra Appl. **604**, 399 (2020).

[42] W. Dai, J. Yuan, and D. Li, Discrete-time quantum walk on the Cayley graph of the dihedral group, Quantum Info. Proc. **17**, 330 (2018).

[43] O. L. Acevedo, and T. Gobron, Quantum walks on Cayley graphs, J. Phys. A: Math. Gen. **39**, 585 (2006).

[44] G. M. D'Ariano, M. Erba, P. Perinotti, and A. Tosini, Virtually abelian quantum walks, J. Phys. A: Math. Theor. **50**, 035301 (2017).

[45] D. S. Dummit and R. M. Foote, *Abstract Algebra*, 3rd ed. (Wiley, Hoboken, NJ, 2004).

[46] Y. Wang, Z. Hu, B. Sanders, and S. Kais, Qudits and high-dimensional quantum computing, Front. Phys. **8**, 589504 (2020).

[47] A. Muthukrishnan and C. R. Stroud, Multivalued logic gates for quantum computation, Phys. Rev. A **62**, 052309 (2000).

[48] A. Fedullo, On the existence of a Hilbert-space model for finite-valued observables, Nuov Cim B **107**, 1413 (1992).

[49] M. A. Nielsen and I. Chuang, *Quantum computation and quantum information* (Cambridge University Press, Cambridge, 2002).

[50] M. Ramzan, and M. K. Khan, Decoherence and entanglement degradation of a qubit-qutrit system in non-inertial frames, Quantum Info. Proc. **11**, 443 (2012).

[51] S. Kullback, and R. A. Leibler, On information and sufficiency, Ann. Math. Stat. **22**, 79 (1951).

[52] D. J. C. MacKay, *Information Theory, Inference, and Learning Algorithms* (3rd printing) (Cambridge University Press, Cambridge, 2004).

[53] D. A. Levin, Y. Peres, and E. L. Wilmer, *Markov Chains and Mixing Times*, 2nd revised ed., (AMS, Providence, 2017).

[54] M. Nakahara and T. Ohmi, *Quantum Computing: From Linear Algebra to Physical Realizations*, 1st ed. (CRC Press, Boca Raton, 2008).